

## Stability of explicit advection schemes. The balance point location rule

B. P. Leonard\*

*Department of Mechanical Engineering, The University of Akron, Akron, OH 44325-3903, U.S.A.*

### SUMMARY

This paper introduces the balance point location rule, providing specific necessary and sufficient conditions for constructing unconditionally stable explicit advection schemes, in both semi-Lagrangian and flux-form Eulerian formulations. The rule determines how the spatial stencil is placed on the computational grid. It requires the balance point (the center of the stencil in index space) to be located in the same patch as the departure point for semi-Lagrangian schemes or the same cell as the sweep point for Eulerian schemes. Centering the stencil in this way guarantees stability, regardless of the size of the time step. In contrast, the original Courant–Friedrichs–Lewy (CFL) condition requiring the stencil merely to include the departure (sweep) point, although necessary, is not sufficient for guaranteeing stability. The CFL condition is of limited practical value, whereas the balance point location rule always gives precise and easily implemented prescriptions for constructing stable algorithms. The rule is also helpful in correcting a number of misconceptions that have arisen concerning explicit advection schemes. In particular, explicit Eulerian schemes are widely believed to be inefficient because of stability constraints on the time step, dictated by a narrow interpretation of the CFL condition requiring the Courant number to be less than or equal to one. However, such constraints apply only to a particular class of advection schemes resulting from centering the stencil on the *arrival* point, when in fact the sole function of the stencil is to estimate the departure (sweep) point value—the arrival point has no relevance in determining the placement of the stencil. Unconditionally stable explicit Eulerian advection schemes are efficient and accurate, comparable in operation count to semi-Lagrangian schemes of the same order, but because of their flux-based formulation, they have the added advantage of being inherently conservative. Copyright © 2002 John Wiley & Sons, Ltd.

KEY WORDS: advection; balance point location rule; CFL condition; Eulerian; semi-Lagrangian; stability

### 1. INTRODUCTION

The primary focus of this paper is on the stability of explicit, flux-based Eulerian advection schemes. In particular, the paper attempts to correct a commonly held belief that such schemes are inefficient because of severe time-step constraints dictated by a narrow (but not generally

---

\* Correspondence to: B. P. Leonard, Department of Mechanical Engineering, The University of Akron, Akron, OH 44325-3903, U.S.A.

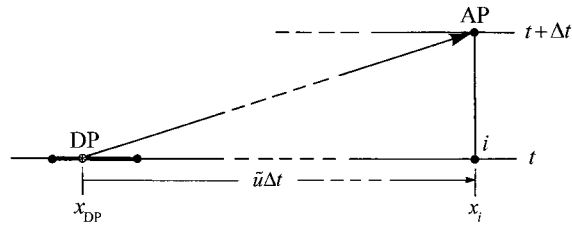


Figure 1. Definition of the departure point (DP) and arrival point (AP) in a space–time portrayal of the advective characteristic in a semi-Lagrangian update. The departure point patch is indicated by the heavy line (and includes the two adjacent grid-points).

valid) interpretation of ‘the CFL condition’, stemming from the often-cited paper by Courant *et al.* [1, 2]. Although a number of papers have appeared showing how to construct unconditionally stable explicit flux-form Eulerian advection schemes [3–6], the belief that Eulerian schemes must satisfy conditional stability constraints remains widespread.

The most common interpretation of the CFL condition is that, for advective stability, the maximum Courant number magnitude should not exceed unity. This is equivalent to requiring a fluid particle to travel not more than one mesh width in one time step, and this is often explained as being a ‘natural’ [7] or ‘physical’ [8] restriction. Since this would indeed place severe constraints on the time step, explicit Eulerian schemes are generally considered to be too expensive for practical calculations. By contrast, it is well known that explicit semi-Lagrangian advection schemes based on tracking individual fluid particles [9] can be constructed so that there are no stability constraints on the time step. In fact, this has been one of the prime motivating factors in the ongoing development of semi-Lagrangian schemes. This apparent circumvention of ‘the CFL condition’ has resulted in some lack of clarity in the literature regarding the relationship between semi-Lagrangian and Eulerian schemes.

In this paper we will see that there is no conflict between the unconditional stability of explicit semi-Lagrangian schemes and the conditional stability of *a very special class of* explicit Eulerian schemes. The apparent difficulty stems from how the computational stencil is located. The common interpretation of the CFL condition—Courant-number-less-than-or-equal-to-one (or, in some cases, less-than-or-equal-to-two)—stems from specifically locating the center of the spatial stencil in the vicinity of the *arrival* point, when seeking information about the *departure* point. (See Figure 1 for the semi-Lagrangian definition of the departure and arrival points and the departure point patch.) This arrival-point-centered stencil defines the special class of Eulerian schemes referred to above. If, however, the spatial stencil is *appropriately* located with respect to the departure point, it is possible to construct stable explicit advection schemes with no restrictions on the time step. The question of just exactly what constitutes appropriate placement is the main subject of this paper.

In semi-Lagrangian terminology, the *original* CFL condition (for advection) merely requires the spatial stencil to be located so that it *includes* the departure point (but, perhaps it should be stressed, not necessarily the arrival point!). Although this is a necessary condition for stability, it is not sufficient nor is it generally helpful for practical guidelines on stable stencil placement. However, by introducing the concept of the balance point defined at the center of the spatial stencil in index space, a much more precise stencil-location rule results.

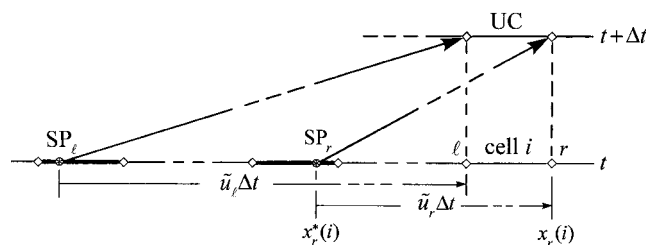


Figure 2. Definition of the left and right sweep points,  $SP_l$  and  $SP_r$ , in a space–time portrayal of the advective characteristics in a flux-integral method. The two sweep point cells are indicated by the heavy lines (and include the respective adjacent faces).

For semi-Lagrangian schemes using explicit forward-in-time integration over a single time step:

The balance point must be located in the same patch as the departure point.

This is both necessary and sufficient for stability without imposing restrictions on the time step. It is a practical prescription for stable stencil placement (and already used intuitively in all successful semi-Lagrangian formulations).

The same type of analysis can be applied to single-time-step explicit Eulerian schemes, using the flux-integral approach [4]. In this case, the sweep point (the foot of the advective characteristic sweeping flux through a particular control-volume face of the update cell, UC) is the analog of the departure point (see Figure 2). The corresponding balance point location rule for each sweep point is:

The balance point must be located in the same cell as the sweep point.

Again, this is both necessary and sufficient for unconditional stability. Unrestricted-time-step explicit flux-integral methods of this type can be very efficient and accurate, and have the additional advantage of being inherently conservative.

For the stability of explicit advection schemes, the *location* of the spatial stencil is all important. The width of the stencil is irrelevant as far as stability is concerned. If the location of the stencil is pre-specified, then the (original) Courant–Friedrichs–Lewy inclusion condition places both upper *and* lower limits on the time step. For some first- and second-order methods, this happens to also be sufficient for stability. However, for third- and higher-order methods, the CFL condition is insufficient for stability and of no practical value. If the pre-specified stencil is required to include the *arrival* point in its *stable* region, this results in the Courant-number-less-than-or-equal-to-one condition (or in some cases, less-than-or-equal-to-two). And this is true *irrespective of the total width* of the stencil! But if the position of the departure point (sweep point) is found first (corresponding to a specified time step), then the location of the spatial stencil can be chosen to satisfy either the Courant–Friedrichs–Lewy condition or the balance point location rule. In general, the former is not specific enough to guarantee stability, whereas the latter always is.

The conditionally stable ‘classical’ explicit Eulerian schemes, having pre-specified stencils specifically moored to the *arrival* point, should be viewed as special cases of the general class of explicit advection schemes discussed in this paper. Because of their severe time-step

restrictions, they are sometimes too inefficient for practical calculations. But unrestricted-time-step explicit Eulerian schemes are easy to construct using the balance point location rule, and (provided higher *odd*-order interpolation is used) are highly computationally efficient.

Although the main focus of the paper is on Eulerian schemes, we will first derive, in the next section, the basic ideas of the balance point location rule within a semi-Lagrangian framework, since the concepts are somewhat simpler and the terminology likely to be more familiar. The idea of ‘centering’ the spatial stencil on the departure point has been in common use in semi-Lagrangian schemes since their inception. However, there has apparently never been any general analysis of why *centering* on the departure point (as opposed to merely *inclusion* of the departure point, as necessitated by the *original* CFL condition) is both necessary and sufficient for stability. Some subtleties regarding significant differences between odd- and even-order schemes are also addressed. In particular, the *need* for choosing between upwind and downwind biasing of the stencil for even-order interpolants is discussed. And conditions relating to *arrival* point centered schemes are clarified.

The development is based on von Neumann stability analysis, assuming a uniform one-dimensional grid and uniform advecting velocity. In order to gain some feeling for estimating the departure point value and the corresponding effect on the overall scheme, a sequence of collocated piecewise-polynomial interpolants is considered, ranging from first-order through fourth-order. Some generalizations to multidimensional grids and other types of interpolants are briefly discussed.

Conservative, flux-based explicit Eulerian schemes are then considered, with a brief review of the flux-integral method. We will see that there is a strong correlation between flux-integral Eulerian schemes and particle-tracking semi-Lagrangian schemes of the same order. Because of this, stability analysis of each Eulerian scheme can be reduced to that of the corresponding semi-Lagrangian scheme, previously considered. Whereas for semi-Lagrangian schemes, the stencil has to be centered on the departure point for interpolating the advected variable directly, for Eulerian schemes, the stencil needs to be centered on the sweep point for interpolation of the flux-integral variable.

Following some concluding remarks, Appendix A summarizes a number of useful recursion relations for generating arbitrarily higher-order methods. This leads to a proof of the balance point location rule in Appendix B.

## 2. THE BALANCE POINT LOCATION RULE

Referring to Figure 1, designate grid-point  $i$  as the arrival point (at  $x_i$ ). An explicit semi-Lagrangian update sets the predicted value of the advected variable at  $i$  equal to the current value at the departure point

$$\phi_i^+ \equiv \phi(x_i, t + \Delta t) = \phi_{\text{DP}} = \phi(x_{\text{DP}}, t) \equiv \phi(x_i - \tilde{u}\Delta t, t) \quad (1)$$

If the departure point happens to fall exactly at a grid-point, then exact point-to-point transfer results. In general, though, the departure point will fall in a patch between two grid-points, and appropriate estimation of the departure point value is required. [We define a patch to be the region between (and including) two adjacent grid-points.] Note that  $\tilde{u}$  in Equation (1) is an average advecting velocity over the time interval  $\Delta t$ . This is usually estimated by an iterative process and will incur some error [9]. This error in the departure-point location is

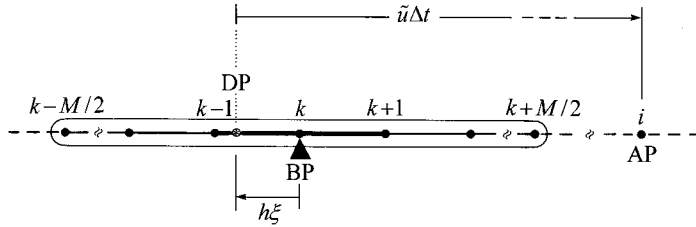


Figure 3. Generic  $\phi$  interpolation stencil for an even-order semi-Lagrangian method.  $M$  is an even integer. The balance point is at grid-point  $k$ . In the case shown, the balance point (BP) has been chosen to be at the *downwind* end of the patch containing the departure point. In this case,  $0 < \xi < 1$ .

quite distinct from the error in the estimation of the departure-point value itself. We assume that  $\tilde{u}$  has been suitably determined [10].

Given the departure point location, suppose that the departure point value is to be estimated using piecewise-polynomial interpolation collocated at an appropriate number of grid-point values. A  $P$ th-degree polynomial requires  $P + 1$  grid-points. In particular, let  $M$  be an even integer. Figure 3 shows an  $(M + 1)$ -point stencil for an  $M$ th-order interpolant. Constant grid spacing,  $h$ , is assumed for simplicity. The stencil is chosen to be well upstream (to the left, for  $\tilde{u} > 0$ ) of the arrival point, grid-point  $i$ , so that there is no pre-specified overlap. The balance point (BP) is defined to be at the center of the stencil, designated here as grid-point  $k$ . As seen in the figure, the stencil extends from  $k - M/2$  to  $k + M/2$ . The relative position of the stencil with respect to the departure point is defined such that the normalized local co-ordinate  $\xi$  is positive for DP anywhere to the left of grid-point  $k$  (and negative to the right). Clearly, from the diagram

$$\tilde{u}\Delta t = h(i - k) + h\xi \tag{2}$$

or, in terms of Courant number

$$c = \frac{\tilde{u}\Delta t}{h} = (i - k) + \xi \tag{3}$$

First, we should be careful to note that the (original) Courant–Friedrichs–Lewy condition requires the departure point to be *included* within the stencil

$$-\frac{M}{2} \leq \xi \leq +\frac{M}{2} \tag{4}$$

Equivalently, in terms of the Courant number

$$(i - k - M/2) \leq c \leq (i - k + M/2) \tag{5}$$

or, in terms of the time step itself

$$(i - k - M/2)\frac{h}{\tilde{u}} \leq \Delta t \leq (i - k + M/2)\frac{h}{\tilde{u}} \tag{6}$$

Note, particularly, the *lower* bound on  $\Delta t$  as well as the upper bound, assuming (as we have) that  $k + M/2 < i$ . On the other hand, if the stencil happens to include the arrival point (i.e.,

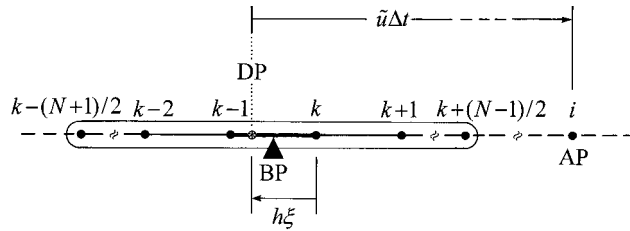


Figure 4. Generic  $\phi$  interpolation for an odd-order semi-Lagrangian method.  $N$  is an odd integer. The balance point is at  $k - \frac{1}{2}$ , at the center of the patch containing the departure point.

if  $k + M/2 \geq i$ , but with  $k \leq i$ , the left-hand side of (6) is no longer positive, so the lower bound becomes simply  $\Delta t > 0$ .

Figure 4 shows the corresponding situation for odd-order schemes. Let  $N$  be an odd integer; the diagram shows an  $(N + 1)$ -point stencil for an  $N$ th-degree collocated polynomial interpolant. In this case, the balance point is midway between two grid-points at the center of the stencil. Choose grid-point  $k$  to be as shown, so that the balance point is at  $(k - \frac{1}{2})$ . Once again, we assume that the stencil is well to the left of the arrival point, grid-point  $i$ . As in the even-order case, Figure 3, the relative position of the stencil with respect to the departure point in Figure 4 is defined by the normalized distance  $\xi$  from grid-point  $k$  to the departure point. In this case, the Courant–Friedrichs–Lewy (inclusion) condition requires

$$-\frac{(N - 1)}{2} \leq \xi \leq \frac{(N + 1)}{2} \tag{7}$$

or, in terms of the Courant number

$$i - k - \frac{(N - 1)}{2} \leq c \leq i - k + \frac{(N + 1)}{2} \tag{8}$$

and, for the time step

$$\left[ i - k - \frac{(N - 1)}{2} \right] \frac{h}{\tilde{u}} \leq \Delta t \leq \left[ i - k + \frac{(N + 1)}{2} \right] \frac{h}{\tilde{u}} \tag{9}$$

once again noting the lower as well as the upper bound on  $\Delta t$ , the former being replaced by  $\Delta t > 0$  if the stencil includes the arrival point.

In order to construct necessary and sufficient conditions for advective stability, we will consider a hierarchy of piecewise polynomials, beginning with a first-order method and proceeding to higher and higher order. Figure 5 shows the first-order situation, a linear interpolant between two adjacent grid-point values. Since this is an odd-order method ( $N = 1$ ), the balance point is located at  $(k - \frac{1}{2})$ , as in the general odd-order case. According to the semi-Lagrangian update, linear interpolation implies

$$\phi_i^+ = \phi_{DP} = \xi \phi_{k-1} + (1 - \xi) \phi_k \tag{10}$$

or, rearranging

$$\phi_i^+ = \phi_k - \xi(\phi_k - \phi_{k-1}) \tag{11}$$

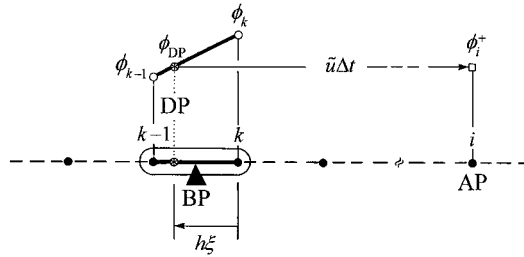


Figure 5. Linear interpolation for a first-order semi-Lagrangian scheme. The balance point is at the center of the departure point patch.

This is equivalent to a first-order ‘upwind’ update of the value at grid-point  $k$  (using an ‘effective’ Courant number of  $\zeta$  over a shorter time interval,  $\delta t = \zeta h / \tilde{u}$ ) followed by point-to-point transfer from  $k$  to  $i$ .

A Fourier–von Neumann analysis follows the evolution of a wave of the form

$$\phi(x, t) = \mathbf{A}(t) \exp(\mathbf{i}\kappa x) \tag{12}$$

where  $\kappa$  is the wavenumber and  $\mathbf{i}$  the imaginary unit. For the exact advection equation

$$\frac{\partial \phi}{\partial t} = -\tilde{u} \frac{\partial \phi}{\partial x} \tag{13}$$

we get, by direct substitution

$$\mathbf{A}'(t) \exp(\mathbf{i}\kappa x) = -\tilde{u} \mathbf{i} \kappa \mathbf{A}(t) \exp(\mathbf{i}\kappa x) \tag{14}$$

This implies a complex amplitude,  $\mathbf{A}(t) = A_0 \exp(-\mathbf{i}\kappa \tilde{u} t)$ . Thus, for the original wave

$$\phi(x, t) = A_0 \exp[\mathbf{i}\kappa(x - \tilde{u}t)] \tag{15}$$

—a travelling wave with a phase speed of  $\tilde{u}$ .

Over a time step  $\Delta t$ , the exact complex amplitude ratio (CAR) is [11]

$$\mathbf{G}_{\text{exact}} = \frac{\phi(x, t + \Delta t)}{\phi(x, t)} = \frac{\mathbf{A}(t + \Delta t)}{\mathbf{A}(t)} = \exp(-\mathbf{i}\kappa \tilde{u} \Delta t) \tag{16}$$

which can be rewritten as

$$\mathbf{G}_{\text{exact}} = \exp(-\mathbf{i}c\theta) = \cos(c\theta) - \mathbf{i} \sin(c\theta) \tag{17}$$

where  $c$  is the Courant number and  $\theta$  the non-dimensional wavenumber

$$\theta = \kappa h \tag{18}$$

In the case of the first-order numerical algorithm, Equation (11), we have

$$\begin{aligned} \phi_i^+ &= \mathbf{A}(t + \Delta t) \exp(\mathbf{i}\kappa x_i) = \mathbf{A}(t) [\exp\{\mathbf{i}\kappa[x_i - (i - k)h]\} \\ &\quad - \zeta (\exp\{\mathbf{i}\kappa[x_i - (i - k)h]\} - \exp\{\mathbf{i}\kappa[x_i - (i - k + 1)h]\})] \end{aligned} \tag{19}$$

This gives a numerical complex amplitude ratio for the first-order semi-Lagrangian scheme

$$\begin{aligned}\mathbf{G}_{\text{SL1}}(c; \theta) &= \frac{\mathbf{A}(t + \Delta t)}{\mathbf{A}(t)} = \exp[-\mathbf{u}(i - \kappa)\theta] \{1 - \xi[1 - \exp(-\mathbf{u}\theta)]\} \\ &= \exp[-\mathbf{u}(i - k)\theta] \mathbf{G}_1(\xi; \theta)\end{aligned}\quad (20)$$

The first factor represents exact point-to-point transfer from grid-point  $k$  to  $i$ . As suggested by the notation, the second factor has the form of a first-order ‘upwind’ CAR for a local update at grid-point  $k$ , using the ‘effective’ Courant number,  $\xi$ .

Stability requires  $|\mathbf{G}_{\text{SL1}}| \leq 1$ . Since the exponential (shift) factor has a magnitude identically equal to 1, we get the condition on the ‘local’ CAR

$$|\mathbf{G}_1| \leq 1 \quad \text{for stability} \quad (21)$$

If we write out  $\mathbf{G}_1$  as a function of  $\xi$ , with  $\theta$  as a parameter

$$\mathbf{G}_1(\xi; \theta) = 1 - \xi(1 - \cos \theta) - \mathbf{u}(\xi \sin \theta) \quad (22)$$

noting that, in general

$$|\mathbf{G}| = \sqrt{[\text{Re}(\mathbf{G})]^2 + [\text{Im}(\mathbf{G})]^2} \quad (23)$$

we find, in this case, that

$$|\mathbf{G}_1| = \sqrt{[1 - 2\xi(1 - \xi)(1 - \cos \theta)]} \quad (24)$$

Figure 6 shows  $|\mathbf{G}_1|$  as a function of  $\xi$ , with  $\theta$  as a parameter ranging from 0 to  $\pi$  rad, in  $20^\circ$  increments. Note that  $\xi$  is shown positive to the left, in order to better correlate with the earlier figures. For  $\theta = \pi$  rad, we see from Equation (22) that  $\mathbf{G}_1$  is real, equal to  $1 - 2\xi$  (negative values of this are shown dashed in the figure); so  $|\mathbf{G}_1| = |1 - 2\xi|$  for  $\theta = \pi$ . From the figure, we see immediately that all wavenumbers are stable for

$$0 \leq \xi \leq 1 \quad (25)$$

and all are unstable for  $\xi < 0$  and  $\xi > 1$ . The unstable regions are shown shaded between  $\theta = 0$  and  $\pi$ . Referring back to Figure 5, this means that, given the location of the departure point in a particular patch, the (two-point) first-order stencil must be located so that the stencil *includes* the departure point—i.e., it covers the same patch. In this case then, the CFL condition happens to be both necessary and sufficient for stability [12].

Another way of describing the stability condition (which, as we will see, is more generally applicable) is in terms of the balance point of the stencil (located at  $k - \frac{1}{2}$  for odd-order schemes), following from (25) and referring to Figure 5:

The balance point must be located in the same patch as the departure point.

This is the balance point location rule for semi-Lagrangian schemes. [It is equivalent to the CFL inclusion condition in this (first-order) case (and will be for second-order, as well). But for third- and higher-order schemes, the balance point location rule gives very specific necessary and sufficient prescriptions for the location of the stencil with respect to the departure point, whereas the Courant–Friedrichs–Lewy condition gives much broader (and only necessary but not sufficient) location bounds.]

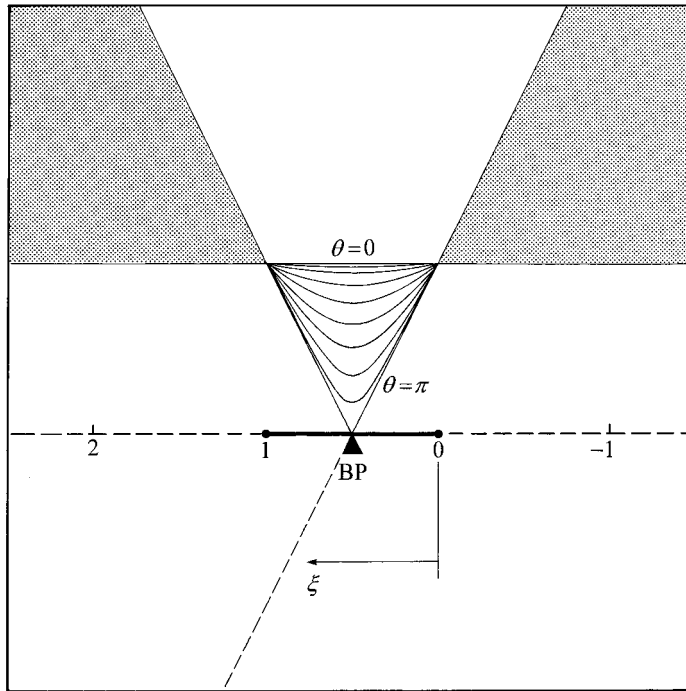


Figure 6. Stability diagram for  $|G_1(\xi; \theta)|$ . The unstable regions are shaded between  $\theta=0$  and  $\pi$  rad. Note the symmetry about  $\xi=0.5$ . The dashed line shows the negative branch of the real-valued line representing the short-wavelength limit,  $G_1(\xi; \pi) = 1 - 2\xi$ .

The phase of a numerical  $\mathbf{G}$  is perhaps best portrayed by the phase error

$$PE = ph(\mathbf{G}_{num}) - ph(\mathbf{G}_{exact}) \tag{26}$$

and since  $\mathbf{G}_{exact} = \exp[-\mathbf{i}(i - k)\theta] \exp(-\mathbf{i}\xi\theta)$ , we see that

$$PE_P = ph(\mathbf{G}_P) - (-\xi\theta) \tag{27}$$

or, more specifically

$$PE_P = \text{artan} \left[ \frac{\text{Im}(\mathbf{G}_P)}{\text{Re}(\mathbf{G}_P)} \right] + \xi\theta \tag{28}$$

where  $\mathbf{G}_P$  is the local CAR for a  $P$ th-order scheme. For the first-order case, we have, from Equation (22)

$$PE_1 = -\text{artan} \left\{ \frac{\xi \sin \theta}{1 - \xi(1 - \cos \theta)} \right\} + \xi\theta \tag{29}$$

where the usual care must be taken regarding the inverse tangent, depending on the quadrant involved in the complex plane.

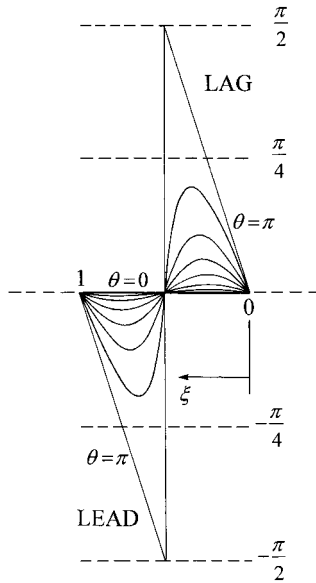


Figure 7. Phase error of the first-order scheme over the stable range,  $0 \leq \xi \leq 1$ , for  $\theta$  ranging between 0 and  $\pi$  rad in  $20^\circ$  increments. The short-wavelength boundaries ( $\theta = \pi$ ) are given by  $PE_1 = \pi\xi$  and  $\pi(\xi - 1)$ .

Figure 7 shows  $PE_1(\xi; \theta)$  for  $\theta = 0$  to  $\pi$  rad in  $20^\circ$  increments over the stable range of  $\xi$ . Note, in particular, that at the short-wavelength limit ( $\theta = \pi, \sin \theta = 0$ ),  $PE_1 = \pi\xi$  or  $\pi(\xi - 1)$ , with a discontinuity at  $\xi = 0.5$ , corresponding to  $\mathbf{G}_1$  passing through zero. Note also that the phase error is zero at  $\xi = 0.5$  for all wavelengths. (These are features common to all *odd-order* schemes.) For  $0 < \xi < 0.5$ , the phase error is positive—this represents phase *lag* (the numerical phase is less negative than the exact phase). And for  $0.5 < \xi < 1$ , we see a corresponding phase *lead*. For odd-order schemes, we will find that the phase error portrait is always antisymmetrical about  $\xi = 0.5$ , with all values contained within the respective triangular regions.

We now turn to a second-order semi-Lagrangian scheme resulting from parabolic interpolation collocated at three adjacent grid-points, as shown in Figure 8. In this case, the semi-Lagrangian update is

$$\phi_i^+ = \phi_{DP} = \phi_k - \frac{\xi}{2}(\phi_{k+1} - \phi_{k-1}) + \frac{\xi^2}{2}(\phi_{k+1} - 2\phi_k + \phi_{k-1}) \tag{30}$$

which could be interpreted as a local second-order ‘central’ or Lax–Wendroff [13] update at grid-point  $k$  using the effective Courant number  $\xi$ , followed by point-to-point transfer from  $k$  to  $i$ . In this case, the semi-Lagrangian complex amplitude ratio is [3]

$$\mathbf{G}_{SL2} = \exp[-\mathbf{u}(i - k)\theta] \mathbf{G}_2 \tag{31}$$

where  $\mathbf{G}_2$  is the local second-order ‘central’ (Lax–Wendroff) CAR

$$\mathbf{G}_2(\xi; \theta) = 1 - \xi^2(1 - \cos \theta) - \mathbf{u}(\xi \sin \theta) \tag{32}$$

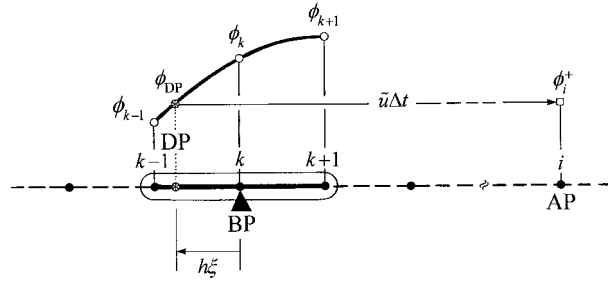


Figure 8. Parabolic interpolation for a second-order semi-Lagrangian scheme. In this case, the balance point has been placed at the *downwind* end of the departure point patch, giving a downwind-biased stencil.

Compare this with the first-order CAR given by Equation (22). Once again, the stability conditions focus on the local CAR,  $|\mathbf{G}_2| \leq 1$ . We find in this case that

$$|\mathbf{G}_2| = \sqrt{[1 - \xi^2(1 - \xi^2)(1 - \cos \theta)]^2} \tag{33}$$

which is shown in Figure 9. From Equation (32), we see that  $\mathbf{G}_2(\xi; \pi) = 1 - 2\xi^2$ ; negative branches of this parabola are shown dashed in the figure. Note that  $|\mathbf{G}_2| = 0$  at the points  $\xi = \pm 1/\sqrt{2}$ . Here, we see immediately from the figure that the second-order semi-Lagrangian scheme is stable for all wavenumbers within the range

$$-1 \leq \xi \leq +1 \tag{34}$$

and unstable for  $\xi < -1$  and  $\xi > +1$ . In other words, the scheme is stable provided we use interpolation (as opposed to extrapolation). Again, this is equivalent to the CFL inclusion condition, which happens to be sufficient in this case, as well.

Referring back to Figure 8, note the significance of positive and negative  $\xi$ . For positive  $\xi$  (the departure point between  $k - 1$  and  $k$ ), the stencil has a *downwind* bias relative to the location of the departure point. This is the situation depicted in Figure 8. For negative  $\xi$ , the stencil is located so that the departure point is between  $k$  and  $k + 1$ , representing an *upwind* bias in the stencil location. Figure 10 shows this situation. In the former case (positive  $\xi$ ), the overall algorithm is equivalent to a local Lax–Wendroff update at grid-point  $k$  (using the effective Courant number  $\xi$ ), followed by point-to-point transfer from  $k$  to  $i$ . In the latter case (negative  $\xi$ ), the overall algorithm is equivalent to a second-order ‘upwind’ update at grid-point  $(k + 1)$  using an effective Courant number of  $(1 - |\xi|)$ , followed by point-to-point transfer from  $(k + 1)$  to  $i$ .

The phase error of the second-order scheme is shown in Figure 11 over the stable range of  $\xi$ . In this case, the phase of  $\mathbf{G}_2(\xi; \pi)$  for positive  $\xi$  (downwind biasing) is  $0$  or  $-\pi$ , and for negative  $\xi$  (upwind biasing), it is  $0$  or  $+\pi$ . Thus, the short-wavelength phase error is  $PE_2 = \pi\xi, \pi(\xi + 1),$  or  $\pi(\xi - 1)$ , with discontinuous jumps where  $\mathbf{G}_2(\xi; \pi)$  passes through zero (at  $\pm 1/\sqrt{2}$ ). For  $0 < \xi < 1$ , the error is overwhelmingly phase lag (with a small portion of very short-wavelength phase lead for  $1/\sqrt{2} < \xi < 1$ ). The figure is antisymmetrical about  $\xi = 0$ , so that an upwind-biased scheme ( $-1 < \xi < 0$ ) typically displays mostly leading phase error. These general features will be found to be typical of all even-order schemes.



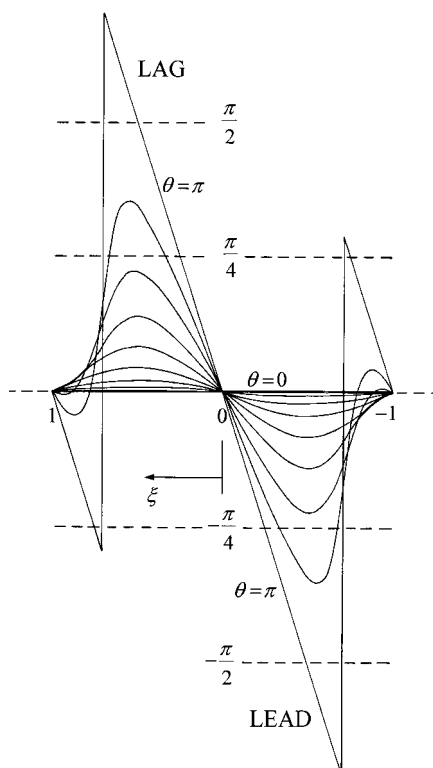


Figure 11. Phase error of second-order scheme over the stable range,  $-1 \leq \zeta \leq +1$ , for  $\theta$  ranging between 0 and  $\pi$  rad. Downwind biasing ( $0 < \zeta \leq 1$ ) correlates with primarily phase lag, whereas upwind biasing ( $-1 \leq \zeta < 0$ ) mostly produces phase lead.

In this case, as seen from Figures 8 and 10, there are two possible locations of the stencil for a given departure point:

- (i) *Downwind biasing*: The balance point (being a grid-point for even-order schemes) is chosen to be at the downwind end of the departure-point patch, Figure 8.
- (ii) *Upwind biasing*: The balance point in this case is chosen to be at the upwind end of the departure point patch, giving the upwind-biased stencil of Figure 10.

In other words, for second-order (and, in fact, all even-order) schemes, we need to make a *velocity-direction-dependent* choice between downwind and upwind biasing because of the *odd* number of interpolation points. In general, downwind biasing is strongly associated with phase-lag numerical dispersion, whereas upwind biasing corresponds to phase lead. Velocity-direction-independent (e.g., odd-order) stencils correlate with very low phase error.

It should perhaps be pointed out that the ‘classical’ Lax–Wendroff scheme uses a downwind-biased stencil (with respect to the departure point). For example, Figure 12 shows the Lax–Wendroff-scheme for  $0 < c \leq 1$ . In this case,  $k = i$  (i.e., the balance point is located at the *arrival* point), and  $\zeta$  is replaced by the actual Courant number,  $c$ . Compare Figures 12

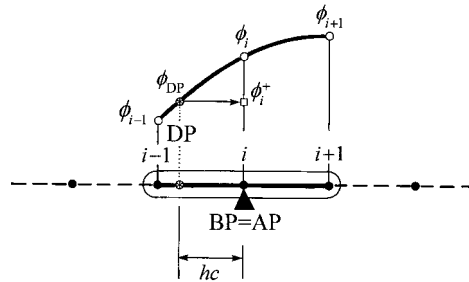


Figure 12. The Lax–Wendroff scheme for  $\tilde{u} > 0$ . Note the downwind biasing of the 3-point stencil with respect to the departure point; BP is at the downwind (right-hand) end of the departure point patch, and this is also the arrival point.

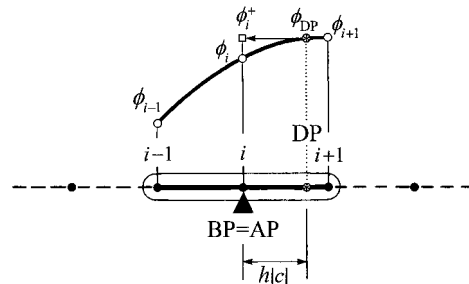


Figure 13. The Lax–Wendroff scheme for  $\tilde{u} < 0$ . Note that there is still a *downwind* bias in the 3-point stencil with respect to the departure point; BP is at the downwind (left-hand) end of the departure point patch, which is still the arrival point.

and 8. If  $-1 \leq c < 0$ , as shown in Figure 13, the stencil is still downwind biased (with respect to the departure point—which is the point at which interpolation takes place), as the velocity is now in the negative direction. The Lax–Wendroff scheme is usually called a second-order ‘central’ scheme because the stencil is centered with respect to the *arrival* point (grid-point  $i$ )—Figures 12 and 13 show the *same* three-point stencil *centered* on grid-point  $i$ . But the arrival point is *totally irrelevant* as far as the interpolation of the departure-point value is concerned. The departure point location is the important point of reference. The Lax–Wendroff scheme (and its well-known concomitant phase-lag dispersion) should be thought of as being associated with a *downwind*-biased stencil (with respect to the departure point).

Alternatively, second-order ‘upwinding’, portrayed in Figure 14 (for  $\tilde{u} > 0$ ), is indeed based on an upwind-biased stencil, at least for  $0 < c < 1$  [3]. In this case, the balance point is at  $i - 1$ . As is well known, second-order upwinding manifests phase-lead dispersion for  $0 < c < 1$ . However, for  $1 < c < 2$ , the scheme shows phase-lag dispersion equivalent to that of a Lax–Wendroff scheme at an effective Courant number of  $(c - 1)$  [3]. The reason for this is easily seen in Figure 15, where the notation implies a local Lax–Wendroff update of the value at grid-point  $(i - 1)$ , using  $\xi = c - 1$ ; then point-to-point transfer from  $i - 1$  to  $i$  [3]. In this

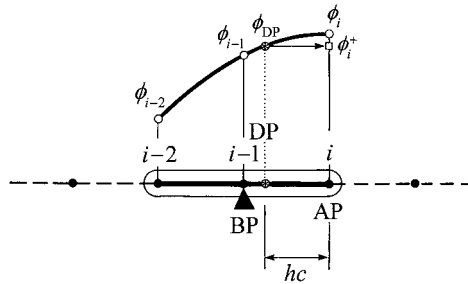


Figure 14. Second-order ‘upwinding’ for  $0 < c < 1$ . Note that the 3-point stencil is indeed *upwind* biased with respect to the departure point; i.e., BP is at the upwind end of the departure point patch at  $i - 1$ .

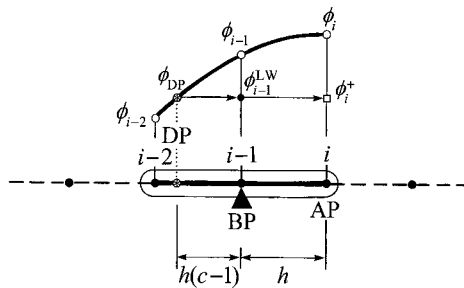


Figure 15. Second-order ‘upwinding’ for  $1 < c < 2$ . Note that, in this case, the 3-point stencil is now *downwind* biased with respect to the departure point. This is equivalent to a Lax–Wendroff update at  $i - 1$ ,  $\phi_i^+ = \phi_{i-1}^{LW} = \phi_{DP}$ .

case, the stencil for the second-order ‘upwind’ scheme is (with respect to the departure point) *downwind* biased!

We should note that the classical Lax–Wendroff scheme is stable for (actual) Courant numbers between  $-1$  and  $+1$ ; i.e., for  $|c| \leq 1$ . Similarly, the second-order-upwind algorithm is stable for  $0 \leq c \leq 2$  for  $\tilde{u} > 0$ , and for  $-2 \leq c \leq 0$  for  $\tilde{u} < 0$ ; in other words, for  $|c| \leq 2$ . These are, of course, just special cases of the general stability conditions given by (34)—for  $\xi = c$  in the former case, and  $\xi = c - 1$  (for  $\tilde{u} > 0$ ) or  $\xi = 1 - |c|$  (for  $\tilde{u} < 0$ ) in the latter. These Courant number restrictions represent severe constraints on the time step. Note that they result from having the balance point of the stencil specifically located in the same patch as the *arrival* point—even though the stencil’s only function is the interpolation of the *departure* point value. The stability of the resulting special class of advection schemes is controlled by what is most commonly called ‘the CFL condition’:  $|c| \leq 1$  for so-called ‘central’ even-order schemes (or, in the case of even-order ‘upwind’ schemes,  $|c| \leq 2$ ). It should be clear from what has been described already that the arrival point should play no role in establishing location conditions on stable placement of the computational stencil. Location of the stencil with respect to the *departure* point is all that matters.

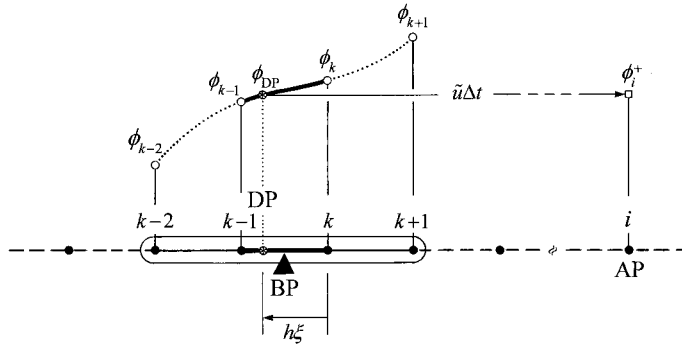


Figure 16. Cubic interpolation for a third-order semi-Lagrangian scheme. The balance point is at the center of the departure point patch.

Moving now to third-order, corresponding to cubic interpolation collocated on a four-point stencil, Figure 16, we find that the explicit semi-Lagrangian update is [14]

$$\begin{aligned} \phi_i^+ = & \phi_k - \frac{\xi}{2}(\phi_{k+1} - \phi_{k-1}) + \frac{\xi^2}{2}(\phi_{k+1} - 2\phi_k + \phi_{k-1}) \\ & + \frac{\xi(1 - \xi^2)}{3!} \left[ \frac{1}{2}(\phi_{k+2} - 2\phi_{k+1} + 2\phi_{k-1} - \phi_{k-2}) \right. \\ & \left. - \frac{1}{2}(\phi_{k+2} - 4\phi_{k+1} + 6\phi_k - 4\phi_{k-1} + \phi_{k-2}) \right] \end{aligned} \quad (35)$$

Note in particular how the update builds on the second-order algorithm, Equation (30). The expression in the square brackets is actually a third difference centered at  $(k - \frac{1}{2})$ , namely  $(\phi_{k+1} - 3\phi_k + 3\phi_{k-1} - \phi_{k-2})$ , rewritten in terms of differences centered at grid-point  $k$ . This notation is useful for comparing higher-order methods. Recursion relations of this type are explored in Appendix A. As usual, the semi-Lagrangian CAR factors into a shift operator (of unity magnitude) multiplied by a local (in this case, third-order) CAR

$$\mathbf{G}_{\text{SL3}} = \exp[-\mathbf{u}(i - k)]\mathbf{G}_3 \quad (36)$$

where  $\mathbf{G}_3$  is given by

$$\begin{aligned} \mathbf{G}_3(\xi; \theta) = & 1 - \xi^2(1 - \cos \theta) - \frac{\xi(1 - \xi^2)}{3}(1 - \cos \theta)^2 \\ & - \mathbf{u} \left[ \xi \sin \theta + \frac{\xi(1 - \xi^2)}{3}(1 - \cos \theta) \sin \theta \right] \end{aligned} \quad (37)$$

From Equation (23), the magnitude is found to be

$$|\mathbf{G}_3| = \sqrt{\{1 - \xi(1 + \xi)(1 - \xi)(2 - \xi)[\frac{1}{3}(1 - \cos \theta)^2 + \frac{2}{9}\xi(1 - \xi)(1 - \cos \theta)^3]\}} \quad (38)$$

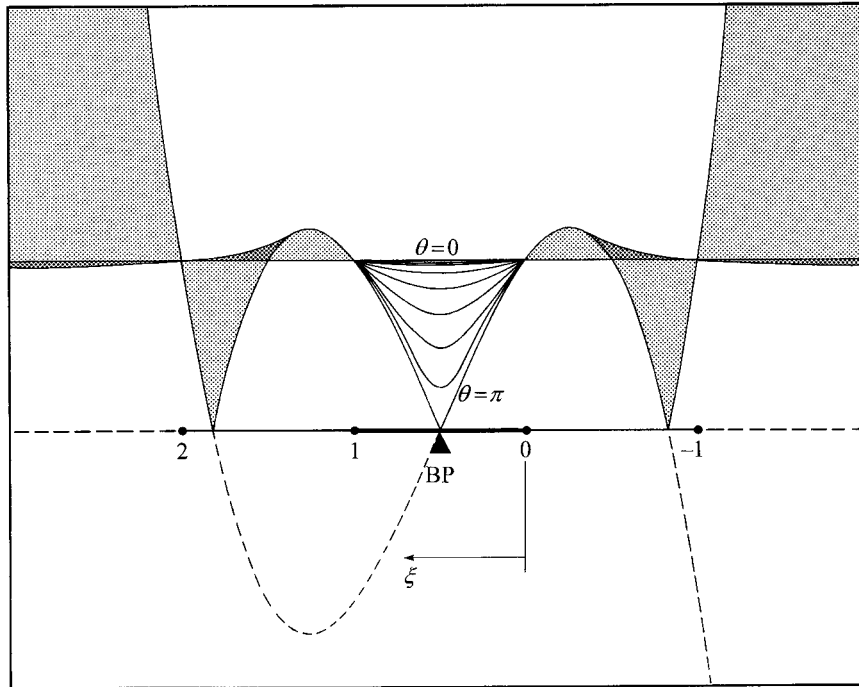


Figure 17. Stability diagram for  $|\mathbf{G}_3(\xi; \theta)|$ . The unstable regions are shaded. Note the symmetry about the balance point at  $\xi = 0.5$ . The dashed curves show the negative branches of the real-valued cubic representing the short-wavelength limit,  $\mathbf{G}_3(\xi; \pi) = 1 - 4/3\xi - 2\xi^2 + 4/3\xi^3$ . On the  $\xi$ -axis, the heavy line shows the stable region, the dashed line signifies extrapolation. Note the isolated stable points,  $\xi = -1$  and  $+2$ .

This is shown in Figure 17 for the usual parameter values. The figure also shows negative branches of the cubic representing real values of  $\mathbf{G}_3(\xi; \pi)$  from Equation (37). Clearly, the only range that is stable for all wavenumbers is

$$0 \leq \xi \leq 1 \tag{39}$$

Instability (at some or all wavenumbers) occurs for  $\xi < 0$  and  $\xi > 1$ , except at the isolated points  $\xi \equiv -1$  and  $2$ , representing exact point-to-point transfer to  $i$  from  $(k + 1)$  and  $(k - 2)$ , respectively. In this case, we see that the CFL condition is not sufficient for stability. For the stencil to include the departure point, we would require

$$-1 \leq \xi \leq 2 \tag{40}$$

which should be compared with the *stability* condition (39). Referring to Figure 16, this implies that, although interpolation (as opposed to extrapolation) is necessary, it is not sufficient; interpolation along the ‘wings’ of the cubic, between  $(k - 2)$  and  $(k - 1)$  or between  $k$  and  $(k + 1)$  in Figure 16, produces an unstable advection algorithm. In terms of practical guidelines for placement of the stencil, the Courant–Friedrichs–Lewy condition is not any more helpful than saying that we are interpolating (rather than extrapolating). But, once again, the balance

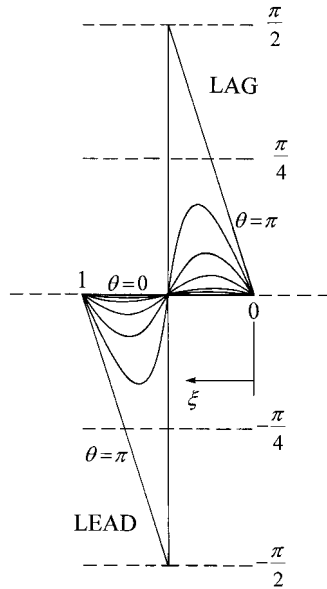


Figure 18. Phase error of the third-order scheme over the stable range,  $0 \leq \xi \leq 1$ , for  $\theta$  between 0 and  $\pi$  rad. Note the similarity to Figure 7 for first-order, but the third-order error is generally much smaller.

point location rule gives a precise (necessary and sufficient) prescription for stable stencil placement:

The balance point must be located in the same patch as the departure point.

For third-order (as with first-order and, as will become clear, all odd-order) schemes, the balance point location rule gives a *unique* prescription for the location of the stencil with respect to the departure point. Only the single central patch of the stencil (containing the balance point) is stable for odd-order advection schemes.

Figure 18 shows the phase-error behavior for the third-order scheme. We immediately see a general similarity with that of the first-order scheme of Figure 7, but note that (except for the short-wavelength limit—which is always the same for any odd-order scheme) the third-order phase error for any given wavenumber is considerably smaller in magnitude. Also, by comparison with Figure 11, it is clear that the third-order phase accuracy is much better than second-order. This is a general trend: odd-order schemes are generally much better behaved in terms of phase accuracy than even order.

Proceeding to higher-order, we now consider a five-point fourth-order stencil involving a collocated quartic, as shown in Figure 19. The explicit update is [14]

$$\begin{aligned} \phi_i^+ = & \phi_k - \frac{\xi}{2}(\phi_{k+1} - \phi_{k-1}) + \frac{\xi^2}{2}(\phi_{k+1} - 2\phi_k + \phi_{k-1}) \\ & + \frac{\xi(1 - \xi^2)}{3!} \left[ \frac{1}{2}(\phi_{k+2} - 2\phi_{k+1} + 2\phi_{k-1} - \phi_{k-2}) \right. \\ & \left. - \frac{\xi}{4}(\phi_{k+2} - 4\phi_{k+1} + 6\phi_k - 4\phi_{k-1} + \phi_{k-2}) \right] \end{aligned} \quad (41)$$

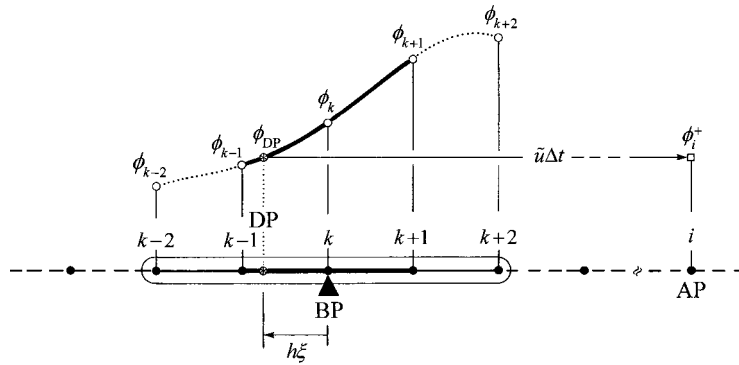


Figure 19. Quartic interpolation for a fourth-order semi-Lagrangian scheme. In this case, the balance point has been placed at the *downwind* end of the departure point patch, giving a downwind-biased stencil.

This should be compared carefully with the third-order update, Equation (35); the two formulas differ only in the coefficient of the fourth difference. (Also see Appendix A for general recursion relations.) The corresponding local fourth-order CAR is given by

$$\begin{aligned}
 \mathbf{G}_4(\xi; \theta) = & 1 - \xi^2(1 - \cos \theta) - \frac{\xi^2(1 - \xi^2)}{6}(1 - \cos \theta)^2 \\
 & - \mathbf{i} \left[ \xi \sin \theta + \frac{\xi(1 - \xi^2)}{3}(1 - \cos \theta) \sin \theta \right] \quad (42)
 \end{aligned}$$

and this should be compared, term-by-term, with the third-order formula, Equation (37). The magnitude, calculated from the general formula, Equation (23), is shown in Figure 20. As usual, because of the common sine factor in the imaginary part,  $\mathbf{G}_4$  is real for  $\theta = \pi$  rad; negative branches of the corresponding quartic representing  $\mathbf{G}_4(\xi; \pi)$  from Equation (42) are shown dashed in the figure. This figure is typical of all higher even-order schemes. Stability at all wavenumbers occurs over a continuous range of  $\xi$  values only within

$$-1 \leq \xi \leq +1 \quad (43)$$

with instability (at some or all wavenumbers) elsewhere, except at specific isolated integer values of  $\xi$  (in this case,  $\xi = \pm 2$ ), reflecting exact point-to-point transfer. The CFL condition would require

$$-2 \leq \xi \leq +2 \quad (44)$$

which, of course, is already required by the fact that we are interpolating. However, only the *two central patches* correspond to stable interpolation; interpolation within the wings of the quartic leads to advective instability. As usual, the balance point location rule gives precise (necessary and sufficient) specification for *stable* interpolation:

The balance point must be located in the same patch as the departure point.

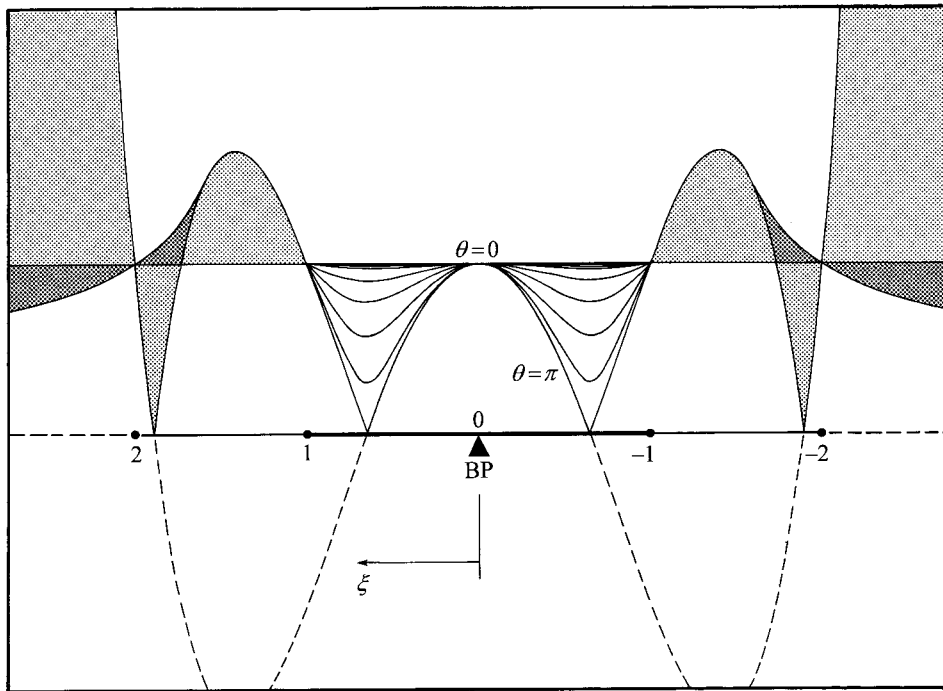


Figure 20. Stability diagram for  $|G_4(\xi; \theta)|$ . The unstable regions are shaded. Note the symmetry about the balance point at  $\xi = 0$ . The dashed curves show negative branches of the real-valued quartic representing the short-wavelength limit,  $G_4(\xi; \pi) = 1 - 8/3\xi - 2\xi^2 + 2/3\xi^4$ . Note the isolated stable points,  $\xi = \pm 2$ .

As with all even-order schemes, the balance point location rule gives two possible locations for stable interpolation, corresponding to downwind biasing of the stencil (the case shown in Figure 19), where the balance point is downwind of the departure point, or upwind biasing, where the balance point (grid-point  $k$ ) would be located at the upwind end of the patch containing the departure point (envisage DP between  $k$  and  $k + 1$ ).

The fourth-order phase error is shown in Figure 21. We see a strong resemblance to the second-order scheme of Figure 11, but (except for  $\theta = \pi$ ) with a smaller (in magnitude) error at any given wavelength. It is instructive to compare the phase error behavior of the schemes considered so far (Figures 7, 11, 18 and 21). The general similarity between the odd-order schemes on the one hand and the even-order schemes on the other is clear. The phase accuracy of any odd-order scheme (e.g., third-order) is seen to be generally much better than that of neighboring even-order schemes (e.g., second- or fourth-order). Numerical simulations confirm this observation [4]. Odd-order results are always very well behaved in terms of phase accuracy, whereas even-order results are plagued with serious numerical dispersion error—phase lag for downwind-biased schemes, phase lead for upwind biasing.

Higher-order schemes follow a predictable pattern. In all odd-order cases, the necessary and sufficient stability conditions are given by

$$0 \leq \xi \leq 1 \quad (\text{odd order}) \quad (45)$$

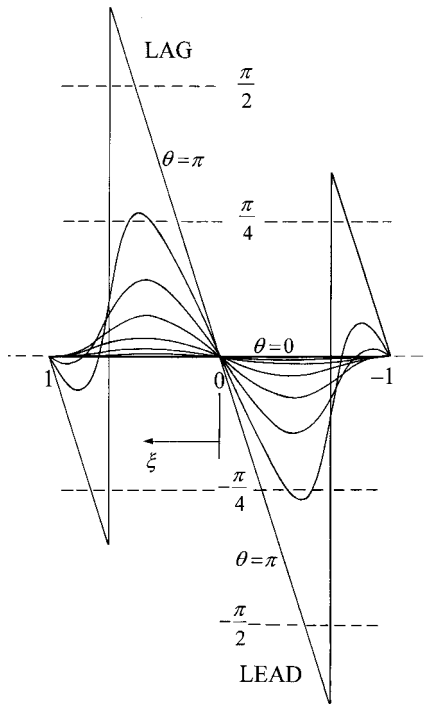


Figure 21. Phase error of the fourth-order scheme over the stable range,  $-1 \leq \xi \leq +1$ , for  $\theta$  between 0 and  $\pi$  rad. Note the similarity to Figure 11 for the second-order. Also note that the error is considerably worse than that of the third-order scheme, Figure 18.

and for all even-order schemes

$$-1 \leq \xi \leq +1 \quad (\text{even order}) \tag{46}$$

Both of these stability conditions are automatically specified by the balance point location rule. The rule gives a unique prescription for locating the stencil with respect to the departure point for stable odd-order schemes. For even-order, there are always two possibilities corresponding to downwind or upwind biasing. Note that, for higher-order schemes, the CFL condition does not discriminate between advectively stable and unstable portions of the interpolation stencil, whereas the balance point location rule does.

So far, we have looked only at one-dimensional semi-Lagrangian schemes. In multidimensions, many semi-Lagrangian formulations use tensor-product piecewise-polynomial interpolants on structured quadrilateral or hexahedral grids. In these cases, the multidimensional complex amplitude ratios factor into a product of one-dimensional components

$$\mathbf{G}_{3D} = \mathbf{G}_x \mathbf{G}_y \mathbf{G}_z \tag{47}$$

Then the balance point location rule applies separately in each co-ordinate direction. Equivalently, we can define a multidimensional balance point at the center of the stencil and two-

dimensional (surface) patches and three-dimensional (volume) patches in an obvious way. The balance point location rule remains the same:

The (multidimensional) balance point must be located in the same  
(multidimensional) patch as the departure point.

As with one-dimensional methods, this gives a unique stencil location for odd-order schemes and  $2^D$  possibilities for even-order, where  $D$  is the dimensionality. So, for multidimensional even-order schemes, we need to make further velocity-component-direction-dependent choices in each co-ordinate direction.

Although we have based the development of the balance point location rule theory on piecewise-polynomial interpolants, it *appears* (judging from the success of semi-Lagrangian schemes) that other forms of interpolants must have closely related stability conditions. For example, multidimensional global interpolants such as cubic splines are very popular (and successful) in many semi-Lagrangian formulations. Odd-order splines are ‘centered’ within each patch in the sense that, in any one co-ordinate direction, for a given patch they use an equal amount of information from both positive and negative directions along the co-ordinate. The ‘balance point’ of the local part of the global stencil is always automatically in the center of the patch being interpolated. Shape-preserving techniques do not seem to corrupt the stability of semi-Lagrangian schemes, provided the underlying basic interpolation is stable.

### 3. CONSERVATIVE EXPLICIT EULERIAN SCHEMES

Until fairly recently, it was generally believed that conservative (flux-form) explicit Eulerian advection schemes, based on a fixed control-volume formulation, were limited to methods governed by the Courant-number-less-than-or-equal-to-one (or, in some cases, two) condition. In 1992, Roache’s ground-breaking paper on the ‘flux-based modified method of characteristics’ [6] showed how to extend conservative explicit Eulerian schemes to large time steps. Although Roache’s formulation was confined to second-order, other publications soon followed, generalizing the large- $\Delta t$  formulation to arbitrarily high-order (including shape preservation) [3, 4] and to multidimensions [5]. The latter schemes are based on the flux-integral concept, which is briefly reviewed here and placed within the context of the balance point location rule.

The formulation begins with the conservative form of the advection equation

$$\frac{\partial \phi}{\partial t} = - \frac{\partial(u\phi)}{\partial x} \quad (48)$$

This is averaged over a control volume of width  $h_i$  and over a time step  $\Delta t$ , giving

$$\frac{\bar{\phi}_i^+ - \bar{\phi}_i}{\Delta t} = \frac{\tilde{u}_\ell \bar{\phi}_\ell - \tilde{u}_r \bar{\phi}_r}{h_i} \quad (49)$$

where the bars signify cell averages,  $\tilde{u}_\ell$  and  $\tilde{u}_r$  are *time-averaged* advecting velocities at the left and right faces of the control volume, and  $\bar{\phi}_\ell$  and  $\bar{\phi}_r$  are also time-averaged face values of the advected variable. The only approximation in Equation (49) is that we have neglected temporal correlations between  $u$  and  $\phi$  at the cell faces (in other words, time-averaged products

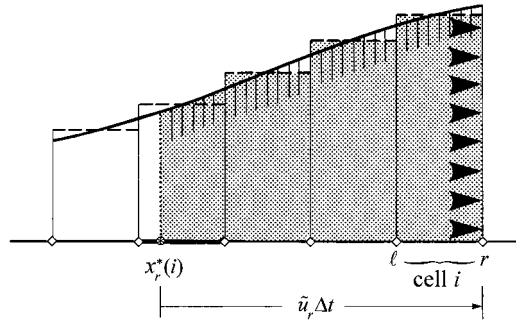


Figure 22. Basic concept of the flux integral method. The shaded area represents the flux of the material through the right face of cell  $i$  in time  $\Delta t$ .

are replaced by products of time averages). We assume that the (time-averaged) advecting velocities at each face are known and *unique* to each face

$$\tilde{u}_r(i) = \tilde{u}_l(i + 1) \quad (\text{known}) \tag{50}$$

Also the (as yet, unknown) time-averaged face values themselves are required to satisfy a face-uniqueness condition

$$\tilde{\phi}_r(i) = \tilde{\phi}_l(i + 1) \quad (\text{to be found}) \tag{51}$$

Equations (50) and (51) taken together guarantee face flux uniqueness, which in turn is responsible for inherent conservation.

If we could *estimate* the (time-averaged) face values, the basic control-volume equation, Equation (49), provides an update algorithm for the *cell-average* values. The flux-integral method is based on estimating subcell behavior,  $\phi(x)$ , satisfying the cell-average constraints

$$\int_{x_l(i)}^{x_r(i)+h_i} \phi(x) dx = h_i \bar{\phi}_i = m_i \quad \text{for all } i \tag{52}$$

introducing the cell ‘material value’,  $m_i$ . If we knew the subcell behavior, we could estimate the amount of ‘material’ being *swept* through the (say, right) face of a given cell in time  $\Delta t$  by calculating the *flux integral*

$$FI_r(i) = \int_0^{\Delta t} \tilde{u}_r \phi_r(t) dt = \int_{x_r(i)-u_r \Delta t}^{x_r(i)} \phi(x) dx = \tilde{u}_r \tilde{\phi}_r \Delta t \tag{53}$$

as suggested in Figure 22. In other words, we have replaced a time integral (representing the average face value) by a spatial integral, making use of the advective characteristic, along which  $\tilde{u}_r dt = dx$ . We perform a similar calculation for each (right) face of every cell, noting that  $FI_l(i) = FI_r(i - 1)$ . Then the updated material value in any cell  $i$  is set equal to the current material value, plus what flows into the cell through the left face, minus what flows out through the right

$$m_i^+ = h_i \bar{\phi}_i^+ = m_i + FI_l(i) - FI_r(i) = h_i \bar{\phi}_i + FI_r(i - 1) - FI_r(i) \tag{54}$$

The most straightforward way of calculating the flux integral in Equation (54) is by introducing the discrete flux-integral variable,  $\psi_i$ , defined *at cell faces* by the cumulative sum

$$\psi_i = \psi_0 + \sum_{p=1}^i m_p = \psi_0 + \sum_{p=1}^i h_p \bar{\phi}_p \quad (55)$$

where  $\psi_i$  occurs at the *right* face of cell  $i$ . Note that any cell material value is given by the difference of discrete  $\psi$  values across the cell

$$m_i = h_i \bar{\phi}_i = \psi_i - \psi_{i-1} \quad (56)$$

Given the discrete  $\psi_i$  values, the next step is to *interpolate*  $\psi$  to give the subcell behavior,  $\psi(x)$ , making sure that the interpolation is *collocated* at the known face values. If we define the subcell behavior of the advected variable to be

$$\phi(x) = \frac{d\psi(x)}{dx} \quad (57)$$

this clearly satisfies the cell-average constraint, Equation (52), because of the collocation of  $\psi(x)$  at cell faces

$$\int_{x_r(i)}^{x_r(i)+h_i} \phi(x) dx = \int_{x_r(i)}^{x_r(i)} \frac{d\psi}{dx} dx = \psi_i - \psi_{i-1} = m_i \quad (58)$$

using Equation (56). With the assumed subcell behavior of  $\psi(x)$ , we are now in a position to evaluate the flux integral

$$FI_r(i) = \int_{x_r^*(i)}^{x_r(i)} \phi(x) dx = \int_{x_r^*(i)}^{x_r(i)} \frac{d\psi(x)}{dx} dx = \int_{\psi(x_r^*)}^{\psi_i} d\psi = \psi_i - \psi(x_r^*) \quad (59)$$

where  $x_r^*(i) = x_r(i) - \tilde{u}_r \Delta t$  is the foot of the advective characteristic sweeping flux through the right face of cell  $i$ , as shown in Figures 2 and 22. This is called the sweep point. The first term on the right of Equation (59) is the (known) discrete  $\psi$  value at the right face of cell  $i$ ; the flux integral algorithm thus hinges on the interpolation of  $\psi(x)$  at the sweep point,  $x_r^*$ .

The flux-integral algorithm can be summarized as follows:

- (i) Given current values of  $m_i$  (or  $\bar{\phi}_i$ ), compute the current discrete  $\psi_i$  values from the running sum, Equation (55); this is done once per time step.
- (ii) Estimate the sweep-point value,  $\psi(x_r^*)$ , for the right face of each cell, using an *appropriate*  $\psi$  interpolation, collocated at the known face values.
- (iii) Compute the flux integral for (the right face of) each cell, using Equation (59); only one flux-integral term per cell is needed because of flux uniqueness.
- (iv) Update  $m_i^+$  (or  $\bar{\phi}_i^+$ ) from Equation (54). If needed, Equation (57) gives  $\phi(x)$ .

Note that the ‘cost’ of the algorithm is in the interpolation of step (ii); the cost of the other steps is negligible. Just what constitutes *appropriate* interpolation in the subject of the remainder of this section. Since there is a strong analogy between flux-integral methods and semi-Lagrangian methods, we will start by stating some general rules for even- and odd-order flux-integral schemes. We will then look at a few examples in order to visualize what’s happening in specific cases, and relate this to the corresponding semi-Lagrangian schemes.

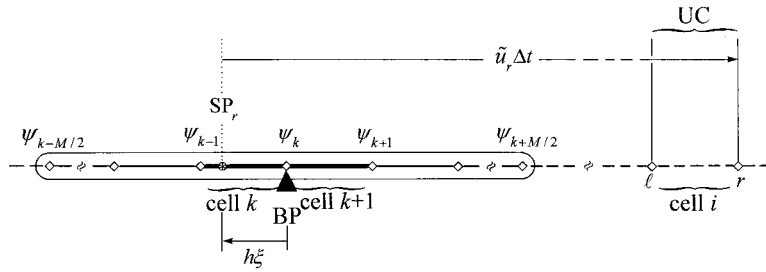


Figure 23. Generic  $\psi$  interpolation stencil for an even-order flux integral method.  $M$  is an even integer. The balance point is at the face common to cells  $k$  and  $k + 1$ . In the case shown, the balance point has been placed at the *downwind* end of the cell containing the sweep point, giving a downwind-biased stencil.

Figure 23 shows an even-order  $\psi$  stencil suitable for an  $M$ th-degree polynomial interpolant for  $\psi(x)$  collocated at discrete  $\psi$  values occurring at  $(M + 1)$  face locations ( $M = \text{even integer}$ ). The balance point is at the center of the  $\psi$  stencil, at the face shared by cell  $k$  and cell  $(k + 1)$ ; this is where  $\psi_k$  occurs. For simplicity, constant cell widths are assumed. The sweep point ( $SP_r$ ) is shown at a distance  $h\xi$  to the left of the right face of cell  $k$ . Figure 23 is the flux-integral analogue of the semi-Lagrangian even-order stencil, Figure 3. Note that when we refer to a particular cell, this also includes *both faces* adjoining the cell; however, the notation for discrete  $\psi$  values indicates that they occur at the *right* face of the corresponding cell. By analogy with the semi-Lagrangian stability analysis, we will anticipate the stability condition for appropriate interpolation by giving the flux-integral balance point location rule:

The balance point must be located in the same cell as the sweep point.

or, equivalently, in terms of  $\xi$ , for even-order schemes

$$-1 \leq \xi \leq +1 \tag{60}$$

This is both necessary and sufficient for stable interpolation of the sweep point value of the flux-integral variable,  $\psi(x_r^*)$ , for even-order methods.

We see (as in the semi-Lagrangian formulation) that for even-order schemes, the balance point location rule allows two possible stencil locations. Figure 23 shows the downwind-biased situation—the balance point is located at the downwind face of the cell containing the sweep point. Upwind biasing occurs when the balance point is located at the upwind face of the cell containing the sweep point; this is easily visualized (imagine  $SP_r$  occurring in cell  $k + 1$ ).

For odd-order schemes, the generalized stencil is shown in Figure 24. In this case, the balance point occurs at the midpoint of the central cell. The relative co-ordinate,  $\xi$ , is measured (positive to the left) from the right face of cell  $k$  to the sweep point. Stable stencil placement is again governed by the balance point location rule:

The balance point must be located in the same cell as the sweep point.

In this odd-order case, this means that  $\xi$  must be in the range

$$0 \leq \xi \leq 1 \tag{61}$$

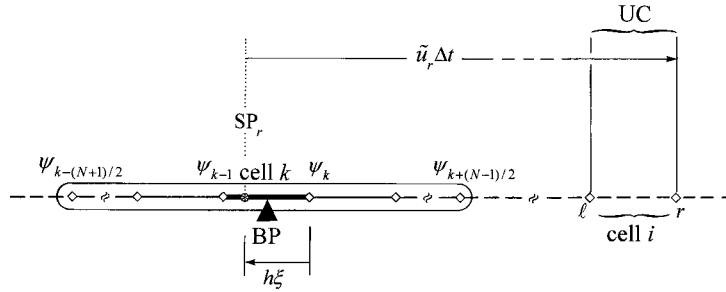


Figure 24. Generic  $\psi$  interpolation stencil for an odd-order flux integral method.  $N$  is an odd integer. The balance point is at the center of cell  $k$ , which contains the sweep point.

This represents both necessary and sufficient conditions for stable interpolation of  $\psi(x_r^*)$ . As in the case of odd-order semi-Lagrangian schemes, the balance point location rule gives a unique prescription for stencil placement for odd-order sweep point interpolation.

In order to get some ‘feel’ for the mechanics of the flux-integral method, we will now run through the details of first-, second-, and third-order methods. And we can see how these relate to the corresponding semi-Lagrangian schemes. In particular, we will see that, under constant-velocity conditions ( $\tilde{u}_l = \tilde{u}_r = \tilde{u} = \text{constant}$ ), the corresponding update algorithms are identical in form. (As a matter of practical importance, the operation count is virtually the same for both methods, even in the variable-velocity case; the flux-integral method, however, has the added advantage of inherent conservation because of the control-volume flux formulation and the flux-uniqueness conditions.)

Figure 25 shows the situation for a first-order flux-integral method. Discrete  $\psi$  values and piecewise-linear  $\psi(x)$  interpolants are shown in part (a) of the figure. Part (b) shows the corresponding piecewise-constant  $\phi(x)$  behavior; in other words,  $\phi(x) = \bar{\phi}_j$  over each cell  $j$ , with discontinuities at cell faces, corresponding to the sudden changes in the slope of  $\psi(x)$ . The amount of material swept through the right face of cell  $i$  consists of an integer number of cell material values from cell  $i$  back to cell  $k + 1$ , plus a portion of the material in cell  $k$ . In order to compute  $FI_r(i)$  from Equation (59), we need the interpolated value  $\psi^* = \psi(x_r^*)$ . We see that the linear interpolation implies

$$\psi^*(i) = \psi_k - \zeta(\psi_k - \psi_{k-1}) = \psi_k - h\zeta\bar{\phi}_k \tag{62}$$

The flux integral is therefore

$$FI_r(i) = \psi_i - [\psi_k - h\zeta\bar{\phi}_k] = \psi_i - \psi_k + h\zeta\bar{\phi}_k = h \sum_{k+1}^i \bar{\phi}_p + h\zeta\bar{\phi}_k = \sum_{k+1}^i m_p + h\zeta\bar{\phi}_k \tag{63}$$

in this case, confirming the above description. In the general (variable-velocity) case, there is a similar calculation for  $FI_l(i) = FI_r(i - 1)$ , and the explicit update proceeds according to Equation (54).

In the constant-velocity case, we can make some further simplifications. In particular, the left-face flux integral for cell  $i$  is

$$FI_l(i) = FI_r(i - 1) = \psi_{i-1} - \psi_{k-1} + h\zeta\bar{\phi}_{k-1} \tag{64}$$

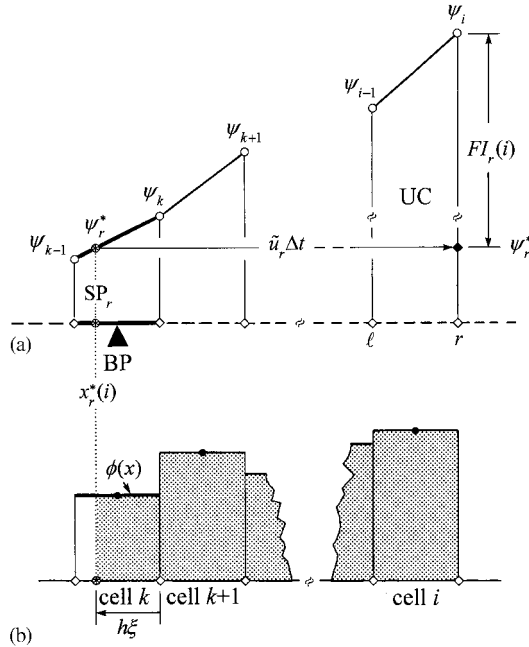


Figure 25. First-order integral method. (a) Piecewise-linear collocated interpolant for  $\psi(x_r^*)$ . (b) Corresponding piecewise-constant  $\phi(x)$ .

Note that the indexes are exactly one less than those of Equation (63) and that  $\zeta$  has the same numerical value for both faces. The constant-velocity update becomes

$$\begin{aligned}
 m_i^+ &= h\bar{\phi}_i^+ = h\bar{\phi}_i + [\psi_{i-1} - \psi_{k-1} + h\zeta\bar{\phi}_{k-1}] - [\psi_i - \psi_k + h\zeta\bar{\phi}_k] \\
 &= h\bar{\phi}_i - (\psi_i - \psi_{i-1}) + (\psi_k - \psi_{k-1}) - h\zeta(\bar{\phi}_k - \bar{\phi}_{k-1}) \\
 &= h\bar{\phi}_i - h\bar{\phi}_i + h\bar{\phi}_k - h\zeta(\bar{\phi}_k - \bar{\phi}_{k-1})
 \end{aligned}
 \tag{65}$$

Cancelling terms and dividing through by  $h$  gives a familiar formula

$$\bar{\phi}_i^+ = \bar{\phi}_k - \zeta(\bar{\phi}_k - \bar{\phi}_{k-1})
 \tag{66}$$

identical in form to the first-order semi-Lagrangian update, Equation (11), with the exception that cell-average values replace nodal-point values. [For first-order (and second-order) flux-integral formulations, nodal-point values are equal to cell-average values; for third- and higher-order schemes, this is not the case.]

A Fourier–von Neumann analysis of Equation (66) leads to the same conclusions as for the semi-Lagrangian stability analysis of Equation (11)

$$0 \leq \zeta \leq 1
 \tag{67}$$

a necessary and sufficient condition for stability of the first-order scheme in the constant-velocity case. For variable velocity, we simply *assume* that the same condition applies to  $\zeta$

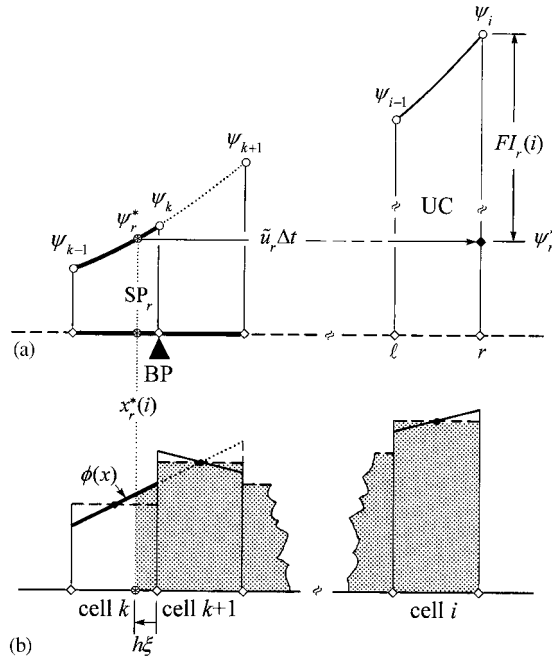


Figure 26. Second-order flux integral method. (a) Downwind-weighted piecewise-parabolic collocated interpolant for  $\psi(x_r^*)$ . (b) Corresponding downwind-weighted piecewise-linear interpolant for  $\phi(x)$ .

for each individual sweep point. This is a common and practical assumption when using the (necessarily constant-velocity) von Neumann stability analysis applied to variable-velocity algorithms. A wide range of computations, at various orders of accuracy, using strongly varying velocity fields, has demonstrated this to be a uniformly successful strategy [5]. In other words, the balance point location rule, applied directly to the  $\psi$  stencil in the variable-velocity case, seems to be entirely satisfactory in establishing stable computations.

We turn now to a second-order interpolation of  $\psi(x)$  shown in Figure 26. The balance point is at the common center face of the two-cell stencil. The case shown corresponds to *downwind* biasing (the balance point is at the downwind face of the sweep point cell). The interpolant for the flux-integral variable,  $\psi(x)$ , is a collocated parabola through  $\psi_{k-1}$ ,  $\psi_k$ , and  $\psi_{k+1}$ . Note how the subcell  $\phi(x)$  is downwind biased; over cell  $k$ , it is a linear interpolant between *node* values  $\bar{\phi}_k$  and (the downwind)  $\bar{\phi}_{k+1}$ . The dotted portions of the interpolants  $\psi(x)$  and  $\phi(x)$  across cell  $k + 1$  do not apply to that cell; instead, a different (downwind-biased) interpolant would be used, as suggested in part (b) of the figure (a linear interpolant between  $\bar{\phi}_{k+1}$  and  $\bar{\phi}_{k+2}$ ).

The quadratic interpolation gives

$$\begin{aligned} \psi^*(i) &= \psi_k - \frac{\xi}{2}(\psi_{k+1} - \psi_{k-1}) + \frac{\xi^2}{2}(\psi_{k+1} - 2\psi_k + \psi_{k-1}) \\ &= \psi_k - \frac{h\xi}{2}(\bar{\phi}_{k+1} + \bar{\phi}_k) + \frac{h\xi^2}{2}(\bar{\phi}_{k+1} - \bar{\phi}_k) \end{aligned} \tag{68}$$

If we proceed directly to the constant-velocity formula, we see

$$h\bar{\phi}_i^+ = h\bar{\phi}_i + \left[ \psi_{i-1} - \psi_{k-1} + \frac{h\xi}{2}(\bar{\phi}_k + \bar{\phi}_{k-1}) - \frac{h\xi^2}{2}(\bar{\phi}_k - \bar{\phi}_{k-1}) \right] \\ - \left[ \psi_i - \psi_k + \frac{h\xi}{2}(\bar{\phi}_{k+1} + \bar{\phi}_k) - \frac{h\xi^2}{2}(\bar{\phi}_{k+1} - \bar{\phi}_k) \right] \quad (69)$$

or, collecting terms and dividing through by  $h$

$$\bar{\phi}_i^+ = \bar{\phi}_k - \frac{\xi}{2}(\bar{\phi}_{k+1} - \bar{\phi}_{k-1}) + \frac{\xi^2}{2}(\bar{\phi}_{k+1} - 2\bar{\phi}_k + \bar{\phi}_{k-1}) \quad (70)$$

identical in form to the second-order semi-Lagrangian update, Equation (30), with node values once again replaced by cell averages. The stability analysis follows directly from Equation (33), so that we have

$$-1 \leq \xi \leq +1 \quad (71)$$

as the necessary and sufficient condition for stability, corresponding to the general balance point location rule for even-order flux-integral methods. Again we assume (with confidence gained through numerical experimentation) that the same conditions apply directly to  $\xi$  for each sweep point evaluation in the variable-velocity case.

Finally, we look at the third-order flux-integral formulation corresponding to a cubic interpolant for  $\psi(x)$  collocated through four adjacent discrete  $\psi$  values, as shown in Figure 27(a). Figure 27(b) then gives the corresponding parabolic interpolant for  $\phi(x) = d\psi/dx$ , showing how the node value within cell  $k$  differs from the cell average. Each three-cell interpolant is used only over the respective central cell, as sketched in the figure. Following the usual procedure, we find that the third-order sweep point value is

$$\psi_i^* = \psi_k - \frac{h\xi}{2}(\bar{\phi}_{k+1} + \bar{\phi}_k) + \frac{\xi^2}{2}(\bar{\phi}_{k+1} - \bar{\phi}_k) + \frac{h\xi(1-\xi^2)}{3!}(\bar{\phi}_{k+1} - 2\bar{\phi}_k + \bar{\phi}_{k-1}) \quad (72)$$

And the corresponding constant-velocity update becomes

$$\bar{\phi}_i^+ = \bar{\phi}_k - \frac{\xi}{2}(\bar{\phi}_{k+1} - \bar{\phi}_{k-1}) + \frac{\xi^2}{2}(\bar{\phi}_{k+1} - 2\bar{\phi}_k + \bar{\phi}_{k-1}) \\ + \frac{\xi(1-\xi^2)}{3!}(\bar{\phi}_{k+1} - 3\bar{\phi}_k + 3\bar{\phi}_{k-1} - \bar{\phi}_{k-2}) \quad (73)$$

identical in form to Equation (35); but in this case,  $\phi_j \equiv \phi(x_j) \neq \bar{\phi}_j$ . The flux-integral stability analysis parallels that of the third-order semi-Lagrangian scheme, resulting in

$$0 \leq \xi \leq 1 \quad (74)$$

as usual for odd-order schemes.

We can already see the strong parallels between the flux-integral formulation and the semi-Lagrangian analysis described in the previous section. Whereas the semi-Lagrangian method focuses on the interpolation of the advected variable at the departure point, the key

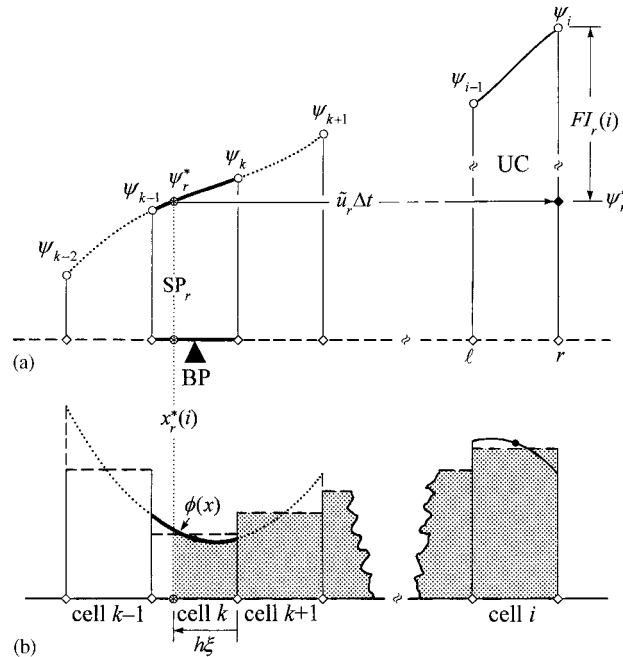


Figure 27. Third-order flux integral method. (a) Piecewise-cubic interpolant for the sweep point  $\psi(x_r^*)$ , collocated at discrete  $\psi$  values located at cell faces. (b) Corresponding subcell piecewise-parabolic interpolant for  $\phi(x)$ .

to the flux-integral method is the interpolation of the flux-integral variable at the sweep point. A  $P$ th-degree polynomial for  $\phi(x)$  collocated at  $P + 1$  nodal points for the discrete  $\phi$  values in the semi-Lagrangian formulation corresponds directly to a  $P$ th-degree polynomial for  $\psi(x)$  collocated at  $P + 1$  face locations for the discrete  $\psi$  values in the flux-integral formulation. In each case, this results in a  $P$ th-order update algorithm. There are two main differences:

- (i) Semi-Lagrangian methods update nodal-point values of the advected variable, whereas flux-integral methods updated cell averages (or material values).
- (ii) Flux-integral methods are inherently conservative in variable-velocity advection fields, whereas most semi-Lagrangian formulations are not.

Multidimensional flux-integral Eulerian schemes are formulated on structured quadrilateral or hexahedral grids. The process is closely related to component-wise operator splitting, but without the concomitant splitting error that that incurs. Naive operator splitting, using conservative-form operators in each co-ordinate direction, results in a form of splitting error called ‘lumpiness’—an initially uniform scalar does not remain uniform in a solenoidal advection field as it must, physically. Details of the construction of multidimensional unrestricted-time-step conservative and constancy-preserving explicit Eulerian advection schemes are fully described in Reference [5].

#### 4. CONCLUSIONS

The stability analysis in this paper has been aimed in part at clearing up some of the inconsistencies in the computational fluid dynamics literature concerning the meaning of the Courant–Friedrichs–Lewy condition as applied to advective modeling. Rephrased in semi-Lagrangian terminology, the original CFL paper simply states that (for advection) the numerical domain of dependence of the arrival point (i.e., the spatial stencil) must *include* the physical domain of dependence of the arrival point (i.e., the single departure point). Although necessary, this is not precise enough to offer practical guidelines for stable stencil placement, especially for higher-order methods involving interpolation stencils wider than one or two mesh widths.

The much more restrictive interpretation of ‘the CFL condition’, i.e., ‘Courant-number-less-than-or-equal-to-one’, appears to have arisen from the primary example discussed in the original paper itself. This involves an *arrival-point-centered, nearest-neighbor* stencil (now known as the Leapfrog scheme)—which, of necessity, results in the  $|c| \leq 1$  condition. This condition *happens to be* the stability requirement for a number of finite-difference methods resulting from subsequent (but relatively early) attempts at explicit modeling of the advection equation; e.g., Lax–Friedrichs [15], Lax–Wendroff, and first-order upwinding, in addition to the Leapfrog scheme itself. Most textbooks that cover the subject discuss the domain-of-dependence argument of the original CFL paper as a necessary condition as well as giving examples of specific *arrival-point-nearest-neighbor* Eulerian schemes, for which  $|c| \leq 1$  is the appropriate stability condition. Unfortunately, a reader may easily get the impression that  $|c| \leq 1$  is *the* stability condition for explicit schemes in general. Some authors reinforce this belief by explaining that this is a ‘natural’ [7] or ‘physical’ [8] constraint. This, in turn, implies severe restrictions on the time step, so that explicit Eulerian schemes are ‘known’ to be very inefficient.

Explicit semi-Lagrangian schemes have become quite popular, largely as a result of the fact that they have no stability restrictions on the time step. In fact, the perceived ‘conditional stability’ of Eulerian schemes has been a prime motivating factor in the development of unconditionally stable semi-Lagrangian schemes. Another reason is that accuracy, especially phase accuracy, is usually very good; this results from the common practice of using *third-order* (particularly cubic-spline) departure point interpolators. Unfortunately, because of the belief that explicit Eulerian schemes are governed by  $|c| \leq 1$ , the unconditional stability of explicit semi-Lagrangian schemes has led to some confusion in the literature. Claims that semi-Lagrangian schemes offer ‘the possibility of using time steps that exceed those permitted by the Courant–Friedrichs–Lewy (CFL) stability criterion for Eulerian discretizations of advection-dominated flows’ [16] and other equivalent statements in the current literature [17–19] demonstrate a common and continuing misuse of the terminology. And one highly regarded modern textbook is perhaps indicative of the problem when it explains that explicit semi-Lagrangian methods ‘cannot be classified as explicit’ [7].

There is another more subtle misconception that can be paraphrased as follows. ‘The CFL condition restricts the time step as a function of the advecting velocity and the *number* of spatial meshes used; as one increases the *size* of the stencil, one can increase the time step’. The concept here is that the interpolating stencil needs to include both the departure point and the arrival point [20]. As seen in this paper, the arrival point is irrelevant in estimating the departure point value. It is not the *size* of the stencil that is important (for stability)—but

its *location* relative to the departure (or sweep) point. Under no circumstances is there any *need* to include the arrival point in the departure point interpolator stencil.

For the purpose of constructing stable algorithms, the original Courant–Friedrichs–Lewy inclusion condition is no more specific than the need to interpolate—which itself (above second-order) cannot guarantee stability. However, we have seen that there is a simple rule for *placement* of the interpolation stencil so as to guarantee stable results. This is based on the concept of the balance point for various types of stencils. For semi-Lagrangian schemes, the balance point is located at the central node of an even-order interpolation stencil or at the mid-point of the central patch of an odd-order stencil. Once the departure point (corresponding to each arrival point) is known, the balance point location rule is very simply stated and implemented:

The balance point must be located in the same patch as the departure point.

This is both necessary and sufficient for the stable construction of semi-Lagrangian algorithms. It gives a unique stencil location for odd-order methods and two possibilities for even-order, corresponding to downwind and upwind biasing. For even-order methods, we must therefore make a further velocity-direction-dependent decision, depending on which type of biasing is preferred. Alternatively, the velocity-direction-independent strategy for even-order methods suggested by Dietachmayer [21] can easily be implemented using the balance point concept: in this case, the balance point must be located *as close as possible* to the departure point [12]. This gives unique placement and is sufficient (though not necessary) for even-order stability. It does not affect the odd-order stencil placement. Note that, because of the sudden switchover between upwinding and downwinding in the even-order case, discontinuities in  $\phi(x)$  will occur in the departure point interpolant midway between grid-points.

Although first-order schemes have been considered here (for demonstration purposes only), it need hardly be said that first-order methods are so artificially numerically diffusive that *they should not be used* for practical calculations. As we have seen, all *even-order* schemes exhibit poor phase accuracy—phase-lag numerical dispersion for downwind-biased schemes and an equally dispersive phase lead for upwind-biased even-order schemes. By distinct contrast, odd-order methods have quite low phase error. Since first-order must be excluded because of its inherent artificial diffusion and all even-order methods should be avoided because of their inherent artificial dispersion, this leaves third-order schemes as the lowest order that should be used for advective modeling.

Third-order interpolants have been very successful in semi-Lagrangian schemes [9] as has the large- $\Delta t$  generalization of the third-order QUICKEST Eulerian scheme [4]. Current research should focus on fifth-order (e.g., quintic spline) or seventh-order interpolants in combination with universal-limiter shape-preservation techniques [4, 5]. Boundary conditions should be handled to the same degree of accuracy as that of the internal algorithm. This is easily achieved by using a type of analytic continuation of the advected variable across the boundary to the appropriate number of external pseudo-nodes (or pseudo-cells). The all too common practice of using low-order, especially first-order, boundary conditions in combination with a higher-order interior method is extremely ill advised.

The special class of schemes that are usually associated with the narrowly restrictive interpretation of ‘the CFL condition’ can be described as follows: the balance point is specifically located in the same patch as the *arrival* point. The list of such schemes would include well-known odd-order so-called ‘upwind’ methods (which are actually based on velocity-

direction-independent interpolator stencils) such as first-order upwinding and the QUICKEST scheme [22], together with even-order so-called ‘central’ schemes (which are actually based on *downwind*-biased departure point interpolator stencils) such as Leapfrog, Lax–Wendroff, fourth-order ‘central’, etc. The latter should be called ‘even-order downwind-biased’ schemes; by contrast, the ‘upwinding’ in the odd-order schemes stems directly from the fact that the departure point is, by definition, *upwind* of the arrival point; the odd-order stencil is independent of velocity direction. All of these schemes are governed by  $|c| \leq 1$ , the most widespread interpretation of ‘the CFL conditions’. The list also includes *even*-order ‘upwind’ schemes (with the balance point at  $i - 1$  for  $\tilde{u} > 0$ ), second-order being the best known. These are governed by  $|c| \leq 2$ . These are truly upwind-biased schemes for  $0 < |c| < 1$ ; but for  $1 < |c| < 2$ , the stencils are actually downwind biased (with respect to the departure point).

Regarding the belief that there is something inherently ‘natural’ or ‘physical’ about constraints on the Courant number to be less than or equal to one, it should now be clear that, on the contrary, it is quite *unnatural* to center the interpolation stencil on the *arrival* point when we are trying to make an estimate of the departure point (or sweep point) value. A fluid particle may cross any number of mesh widths in a single time step—provided the information it carries has been obtained by appropriate means; i.e., by stable departure point (or sweep point) centered interpolation.

Roache’s paper in 1992 laid the ground-work for the development of unconstrained- $\Delta t$  Eulerian advection schemes using higher-order shape-preserving techniques, equal in efficiency to comparable semi-Lagrangian schemes, but with the added advantage of inherent conservation due to the flux-based formulation. Using the flux-integral formulation, the main point of which is the evaluation of the sweep point value of the flux-integral variable, we have seen that the balance point location rule can be used to establish an appropriate sweep point stencil placement strategy.

The balance point must be located in the same cell as the sweep point.

Again, this is both necessary and sufficient for the construction of stable explicit algorithms. For even-order Eulerian schemes, the balance point sits at a control-volume face at the center of the stencil; for odd-order it is at the mid-point of the central cell. As in the semi-Lagrangian formulation, the balance point location rule for flux-integral Eulerian methods gives a unique stencil location for odd-order sweep point interpolators and two possibilities for even-order, corresponding to downwind and upwind biasing. Perhaps a procedure analogous to the Dietachmeyer strategy might be contemplated. However, this results in mid-cell discontinuities in  $\psi(x)$ , implying delta-functions in  $\phi(x)$ . This complexity seems unwarranted, especially when odd-order methods are so much better behaved in terms of phase accuracy.

In summary, it appears that the Courant–Friedrichs–Lewy condition—both the original inclusion condition and the commonly held narrow interpretation,  $|c| \leq 1$  (or  $|c| \leq 2$  in some cases)—should be considered as being of historical interest but of little practical importance in advective modeling. It is perhaps significant that in most semi-Lagrangian literature, reference to ‘the CFL condition’ rarely arises—except in relation to the supposed shortcomings of Eulerian schemes! Once one realizes that the arrival point is irrelevant in constructing the explicit update algorithm and that departure point (or sweep point) interpolator stencil centering is the key to a stable computation, all the mystery and apparent conflicts surrounding ‘the CFL condition’ evaporate.

APPENDIX A. RECURSION RELATIONS FOR HIGHER-ORDER METHODS

Tables AI and AII show a list of (a slight variation on) the well-known coefficients of Pascal's triangle and a related set of coefficients, respectively. The entry in any position in any row (below the first) can be obtained by *subtracting* the left-adjacent entry from the right-adjacent entry in the row above. Clearly, the tables can be extended recursively to arbitrarily high-order. These form a handy compilation of coefficients appearing in various difference formulas, discussed below.

A.1. Fourier-von Neumann transforms

We consider a wave, registered with respect to the arrival point, grid-point  $i$ , with an amplitude normalized to one:  $\exp[\mathbf{i}\kappa(x - x_i)]$ . Then we have the following:

$$\phi_i = 1, \quad \phi_{i-1} = \exp(-\mathbf{i}\theta), \quad \phi_{i-2} = \exp(-2\mathbf{i}\theta) \tag{A1}$$

In particular

$$\phi_{k \pm m} = \exp[-\mathbf{i}(i - k)\theta] \exp(\pm \mathbf{i}m\theta) \tag{A2}$$

For the *local* complex amplitude ratios used in this paper, we are concerned with the second factor. We therefore make the association

$$\phi_{k \pm m} \Rightarrow \exp(\pm \mathbf{i}m\theta) = \cos(m\theta) \pm \mathbf{i} \sin(m\theta) \tag{A3}$$

Table AI. Pascal's triangle.

0		0	0	0	0	0	+1		0	0	0	0	
1	0		0	0	0	+1		-1		0	0	0	
2		0	0	0	+1		-2	+1		0	0	0	
3	0		0	+1	+1	-3		+3		-1	0	0	
4		0		+1	+1	-4	+6		-4	+1		0	
5	0		+1	+1	-5	+10		-10	+5		-1	0	
6		+1		-6	+15		-20	+15		-6	+1		
7	+1		-7		+21		-35		+35		-21	+7	-1
.													
.	.	.	.	.	.	.	.	.	.	.	.	.	.
.													

Table AII. Related triangle.

0	0	0	0	0	0	+1	+1	0	0	0	0	0	0
1		0	0	0	0	+1		0	-1		0	0	0
2	0		0	0	+1		-1		-1	+1		0	0
3		0		0	+1	-2		0	+2		-1	0	0
4	0		0	+1	+1	-3	+2		+2	-3	+1		0
5		0		+1	+1	-4	+5	0	-5		+4	-1	0
6	0		+1	+1	-5	+9		-5	-5	+9		-5	+1
7		+1		-6	+14		-14	0	+14		-14	+6	-1
.													
.	.	.	.	.	.	.	.	.	.	.	.	.	.
.													

Now we list a number of difference expressions and their associated transforms, making use of the coefficients in Tables AI and AII. The so-called binomial coefficients appearing in the following even-order differences are well known. Above first-order, the odd-order coefficients are perhaps less well known, but they can be read directly from Table AII (noting the factor of  $\frac{1}{2}$  in each expression). Note that the trigonometric expressions can always be reduced to products of  $\mathbf{i} \sin \theta$  and powers of  $[-2(1 - \cos \theta)]$ .

First difference centered at  $k$

$$\frac{1}{2}(\phi_{k+1} - \phi_{k-1}) \Rightarrow \mathbf{i} \sin \theta \quad (\text{A4})$$

Second difference centered at  $k$

$$\phi_{k+1} - 2\phi_k + \phi_{k-1} \Rightarrow [-2(1 - \cos \theta)] \quad (\text{A5})$$

Third difference centered at  $k$

$$\frac{1}{2}(\phi_{k+2} - 2\phi_{k+1} + 2\phi_{k-1} - \phi_{k-2}) \Rightarrow \mathbf{i} \sin \theta [-2(1 - \cos \theta)] \quad (\text{A6})$$

Fourth difference centered at  $k$

$$\phi_{k+2} - 4\phi_{k+1} + 6\phi_k - 4\phi_{k-1} + \phi_{k-2} \Rightarrow [-2(1 - \cos \theta)]^2 \quad (\text{A7})$$

Fifth difference centered at  $k$

$$\frac{1}{2}(\phi_{k+3} - 4\phi_{k+2} + 5\phi_{k+1} - 5\phi_{k-1} + 4\phi_{k-2} - \phi_{k-3}) \Rightarrow \mathbf{i} \sin \theta [-2(1 - \cos \theta)]^2 \quad (\text{A8})$$

Sixth difference centered at  $k$

$$\phi_{k+3} - 6\phi_{k+2} + 15\phi_{k+1} - 20\phi_k + 15\phi_{k-1} - 6\phi_{k-2} + \phi_{k-3} \Rightarrow [-2(1 - \cos \theta)]^3 \quad (\text{A9})$$

And this can be continued to arbitrarily higher-order differences.

It is easy to see the pattern in these successively higher-order differences. Let  $M$  be an even integer. Then the  $M$ th difference centered at  $k$  has a (real) transform

$$M\text{th difference} \Rightarrow [-2(1 - \cos \theta)]^{M/2} \quad (\text{A10})$$

and the  $(M + 1)$ st difference centered at  $k$  has a (pure imaginary) transform

$$(M + 1)\text{st difference} \Rightarrow \mathbf{i} \sin \theta [-2(1 - \cos \theta)]^{M/2} \quad (\text{A11})$$

### A.2. Explicit semi-Lagrangian updates

We now list a series of explicit semi-Lagrangian update formulas, beginning with first-order and continuing recursively to higher and higher order. All the differences occurring in the even-order updates are centered at grid-point  $k$  (the balance point). The highest-order difference in each of the odd-order updates is centered at  $k - \frac{1}{2}$  (the position of the balance point for odd-order semi-Lagrangian stencils), but the lower-order differences in odd-order updates are centered at  $k$ . For consistency, and in order to see the recursive relationships between successive orders, we rewrite the odd-order differences as the difference of two differences centered at  $k$ . Some examples will illustrate this notation. The descriptions assume that  $\tilde{u} > 0$ . If  $\tilde{u} < 0$ , the terms ‘upwind’ and ‘downwind’ should be interchanged.

### A.2.1. First-order

$$\phi_i^+(1\text{st}) = \phi_k - \zeta(\phi_k - \phi_{k-1}) \quad (\text{A12})$$

or, rewriting the  $(k - \frac{1}{2})$ -centered first difference

$$\phi_i^+(1\text{st}) = \phi_k - \zeta \left[ \frac{1}{2}(\phi_{k+1} - \phi_{k-1}) - \frac{1}{2}(\phi_{k+1} - 2\phi_k + \phi_{k-1}) \right] \quad (\text{A13})$$

valid for  $0 \leq \zeta \leq 1$ .

### A.2.2. Second-order

$$\phi_i^+(2\text{nd}) = \phi_k - \zeta \left[ \frac{1}{2}(\phi_{k+1} - \phi_{k-1}) - \frac{\zeta}{2}(\phi_{k+1} - 2\phi_k + \phi_{k-1}) \right] \quad (\text{A14})$$

valid for  $-1 \leq \zeta \leq 0$  (upwind biasing) and  $0 \leq \zeta \leq +1$  (downwind biasing). Note the strong similarity between Equations (A13) and (A14); the formulas differ only in one coefficient.

### A.2.3. Third-order

$$\begin{aligned} \phi_i^+(3\text{rd}) = \phi_k - \zeta \left[ \frac{1}{2}(\phi_{k+1} - \phi_{k-1}) - \frac{\zeta}{2}(\phi_{k+1} - 2\phi_k + \phi_{k-1}) \right] \\ + \frac{\zeta(1 - \zeta^2)}{3!}(\phi_{k+1} - 3\phi_k + 3\phi_{k-1} - \phi_{k-2}) \end{aligned} \quad (\text{A15})$$

The  $(k - \frac{1}{2})$ -centered third difference is then rewritten as the difference between a  $k$ -centered third difference and half a  $k$ -centered fourth difference. Since the first terms on the right-hand side constitute the second-order update, we rewrite the third-order formula in recursive form as

$$\begin{aligned} \phi_i^+(3\text{rd}) = \phi_i^+(2\text{nd}) + \frac{\zeta(1 - \zeta^2)}{3!} \left[ \frac{1}{2}(\phi_{k+2} - 2\phi_{k+1} + 2\phi_{k-1} - \phi_{k-2}) \right. \\ \left. - \frac{1}{2}(\phi_{k+2} - 4\phi_{k+1} + 6\phi_k - 4\phi_{k-1} + \phi_{k-2}) \right] \end{aligned} \quad (\text{A16})$$

### A.2.4. Fourth-order. We go straight to the recursive form

$$\begin{aligned} \phi_i^+(3\text{rd}) = \phi_i^+(2\text{nd}) + \frac{\zeta(1 - \zeta^2)}{3!} \left[ \frac{1}{2}(\phi_{k+2} - 2\phi_{k+1} + 2\phi_{k-1} - \phi_{k-2}) \right. \\ \left. - \frac{\zeta}{4}(\phi_{k+2} - 4\phi_{k+1} + 6\phi_k - 4\phi_{k-1} + \phi_{k-2}) \right] \end{aligned} \quad (\text{A17})$$

Carefully compare the coefficients of the last terms in each of Equations (A16) and (A17). A recursive pattern is beginning to become discernible.

### A.2.5. Fifth-order

$$\begin{aligned} \phi_i^+(5\text{th}) &= \phi_i^+(4\text{th}) \\ &- \frac{\xi(1-\xi^2)(4-\xi^2)}{5!} \left[ \frac{1}{2}(\phi_{k+3} - 4\phi_{k+2} + 5\phi_{k+1} - 5\phi_{k-1} + 4\phi_{k-2} - \phi_{k-3}) \right. \\ &\left. - \frac{1}{2}(\phi_{k+3} - 6\phi_{k+2} + 15\phi_{k+1} - 20\phi_k + 15\phi_{k-1} - 6\phi_{k-2} + \phi_{k-3}) \right] \end{aligned} \quad (\text{A18})$$

### A.2.6. Sixth-order

$$\begin{aligned} \phi_i^+(5\text{th}) &= \phi_i^+(4\text{th}) \\ &- \frac{\xi(1-\xi^2)(4-\xi^2)}{5!} \left[ \frac{1}{2}(\phi_{k+3} - 4\phi_{k+2} + 5\phi_{k+1} - 5\phi_{k-1} + 4\phi_{k-2} - \phi_{k-3}) \right. \\ &\left. - \frac{\xi}{6}(\phi_{k+3} - 6\phi_{k+2} + 15\phi_{k+1} - 20\phi_k + 15\phi_{k-1} - 6\phi_{k-2} + \phi_{k-3}) \right] \end{aligned} \quad (\text{A19})$$

### A.3. Generalized recursion relations

The recursive pattern has become clear. We can now *write down* recursive formulas for arbitrarily high-order semi-Lagrangian updates. Let  $N$  be an odd integer and  $M$  an even integer. The odd- $N$ th-order recursive update formula (for  $N \geq 3$ ) has the form

$$\begin{aligned} \phi_i^+(N\text{th}) &= \phi_i^+[(N-1)\text{st}] \\ &- \frac{\xi}{N!} \prod_{p=1}^{(N-1)/2} (\xi^2 - p^2) \left\{ [N\text{th diff}]_k - \frac{1}{2}[(N+1)\text{st diff}]_k \right\} \end{aligned} \quad (\text{A20})$$

where the notation implies differences centered at  $k$ , as we have seen in the examples.

The even-order recursive update formula (for  $M \geq 4$ ) is

$$\begin{aligned} \phi_i^+(M\text{th}) &= \phi_i^+[(M-2)\text{nd}] \\ &- \frac{\xi}{(M-1)!} \prod_{p=1}^{M/2-1} (\xi^2 - p^2) \left\{ [(M-1)\text{st diff}]_k - \frac{\xi}{M}[M\text{th diff}]_k \right\} \end{aligned} \quad (\text{A21})$$

### A.4. Complex amplitude ratios

We can now *write down* successive (local) CARs in a format consistent with recursive generation of higher-order formulas, using the von Neumann transforms derived earlier.

$$\mathbf{G}_1 = 1 + \xi \left\{ \frac{1}{2}[-2(1 - \cos \theta)] - \mathbf{i} \sin \theta \right\} \quad (\text{A22})$$

$$\mathbf{G}_2 = 1 + \xi \left\{ \frac{\xi}{2} [-2(1 - \cos \theta)] - \mathbf{i} \sin \theta \right\} \quad (\text{A23})$$

$$\mathbf{G}_3 = \mathbf{G}_2 + \frac{\xi(\xi^2 - 1^2)}{3!} \left\{ \frac{1}{2} [-2(1 - \cos \theta)]^2 - \mathbf{i} \sin \theta [-2(1 - \cos \theta)] \right\} \quad (\text{A24})$$

$$\mathbf{G}_4 = \mathbf{G}_2 + \frac{\xi(\xi^2 - 1^2)}{3!} \left\{ \frac{\xi}{4} [-2(1 - \cos \theta)]^2 - \mathbf{i} \sin \theta [-2(1 - \cos \theta)] \right\} \quad (\text{A25})$$

$$\mathbf{G}_5 = \mathbf{G}_4 + \frac{\xi(\xi^2 - 1^2)(\xi^2 - 2^2)}{5!} \left\{ \frac{1}{2} [-2(1 - \cos \theta)]^3 - \mathbf{i} \sin \theta [-2(1 - \cos \theta)]^2 \right\} \quad (\text{A26})$$

$$\mathbf{G}_6 = \mathbf{G}_4 + \frac{\xi(\xi^2 - 1^2)(\xi^2 - 2^2)}{5!} \left\{ \frac{\xi}{6} [-2(1 - \cos \theta)]^3 - \mathbf{i} \sin \theta [-2(1 - \cos \theta)]^2 \right\} \quad (\text{A27})$$

$$\mathbf{G}_7 = \mathbf{G}_6 + \frac{\xi(\xi^2 - 1^2)(\xi^2 - 2^2)(\xi^2 - 3^2)}{7!} \left\{ \frac{1}{2} [-2(1 - \cos \theta)]^4 - \mathbf{i} \sin \theta [-2(1 - \cos \theta)]^3 \right\} \quad (\text{A28})$$

$$\mathbf{G}_8 = \mathbf{G}_6 + \frac{\xi(\xi^2 - 1^2)(\xi^2 - 2^2)(\xi^2 - 3^2)}{7!} \left\{ \frac{\xi}{8} [-2(1 - \cos \theta)]^4 - \mathbf{i} \sin \theta [-2(1 - \cos \theta)]^3 \right\} \quad (\text{A29})$$

The recursive pattern is clear, following directly from expressions developed earlier in this appendix. For  $N$  an odd integer ( $N \geq 3$ ) and  $M$  even ( $M \geq 4$ ), we can write general recursive relations as follows. For odd-order

$$\begin{aligned} \mathbf{G}_N &= \mathbf{G}_{N-1} + \frac{\xi}{N!} \prod_{p=1}^{(N-1)/2} (\xi^2 - p^2) \\ &\times \left\{ \frac{1}{2} [-2(1 - \cos \theta)]^{(N+1)/2} - \mathbf{i} \sin \theta [-2(1 - \cos \theta)]^{(N-1)/2} \right\} \end{aligned} \quad (\text{A30})$$

and for even-order

$$\begin{aligned} \mathbf{G}_M &= \mathbf{G}_{M-2} + \frac{\xi}{(M-1)!} \prod_{p=1}^{M/2-1} (\xi^2 - p^2) \\ &\times \left\{ \frac{\xi}{M} [-2(1 - \cos \theta)]^{M/2} - \mathbf{i} \sin \theta [-2(1 - \cos \theta)]^{M/2-1} \right\} \end{aligned} \quad (\text{A31})$$

From Equations (A22)–(A31), we see that the expression for  $\mathbf{G}_P$  is a complex  $P$ th-degree polynomial in  $\xi$ . Note that at the short-wavelength cutoff, when  $\theta = \pi$  rad ( $\sin \pi = 0$ ,  $\cos \pi = -1$ ),  $\mathbf{G}_P$  is a *real*-valued  $P$ th-degree polynomial.

APPENDIX B. PROOF OF THE STABILITY CONDITIONS

We begin by looking at the behavior of  $\mathbf{G}^2$  for the local CARs. In general

$$\mathbf{G}^2 = [\text{Re}(\mathbf{G})]^2 + [\text{Im}(\mathbf{G})]^2 \tag{B1}$$

In Appendix A, we saw that a  $P$ th-order CAR,  $\mathbf{G}_P$ , is a  $P$ th-degree polynomial in  $\xi$  with (complex) coefficients involving products of  $\sin \theta$  powers of  $[-2(1 - \cos \theta)]$ . Thus,  $\mathbf{G}_P^2$  is a polynomial in  $\xi$  of degree  $2P$  with real coefficients. For reference, we show here plots of  $\mathbf{G}_P^2$  versus  $\xi$  (with  $\theta$  ranging from 0 to  $\pi$  rad) for  $P$  equal to 1 through 4; the unstable regions are shown shaded for  $\theta$  between 0 and  $\pi$ .

In Figures B1, B2, B3 and B4, we notice several properties that extend to higher-order because of the recursive nature of the structure of the  $\mathbf{G}$  (and  $\mathbf{G}^2$ ) formulas:

- (i) All odd-order  $\mathbf{G}^2$  plots are symmetrical about  $\xi = 0.5$ .
- (ii) All even-order  $\mathbf{G}^2$  plots are symmetrical about  $\xi = 0$ .
- (iii) For  $N$  equal to an odd integer,  $\mathbf{G}_N^2 \equiv 1$  at all integer values of  $\xi$  from  $-(N - 1)/2$  to  $(N + 1)/2$ .
- (iv) For  $M$  equal to an even integer,  $\mathbf{G}_M^2 \equiv 1$  at all integer values of  $\xi$  from  $-M/2$  to  $+M/2$ .
- (v) The odd-order  $\mathbf{G}^2$  plots all have a single turning point for  $\xi$  between 0 and 1 (at  $\xi = 0.5$ ).
- (vi) The even-order  $\mathbf{G}^2$  plots all have a single turning point for  $\xi$  between 0 and 1; and again, by symmetry, between 0 and  $-1$ .

These properties guarantee stability at all wavenumbers ( $0 \leq \theta \leq \pi$ ) for  $0 \leq \xi \leq 1$  for odd-order schemes, and  $-1 \leq \xi \leq +1$  for even-order schemes. In other words, these ranges of  $\xi$  are

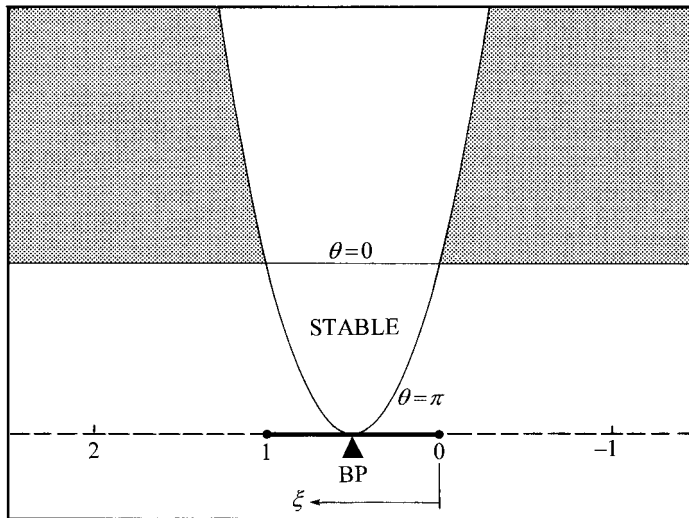


Figure B1. First-order  $\mathbf{G}_1^2(\xi; \theta)$  as a function of  $\xi$ , with  $\theta$  as a parameter.

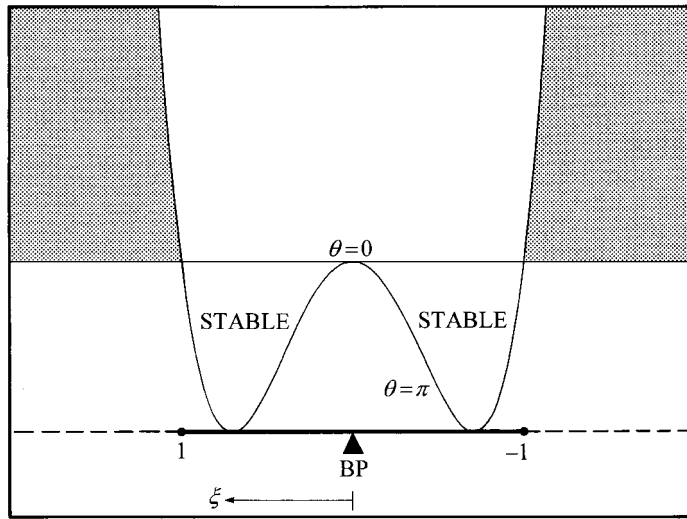


Figure B2. Second-order  $G_2^2(\xi; \theta)$  as a function of  $\xi$ , with  $\theta$  as a parameter.

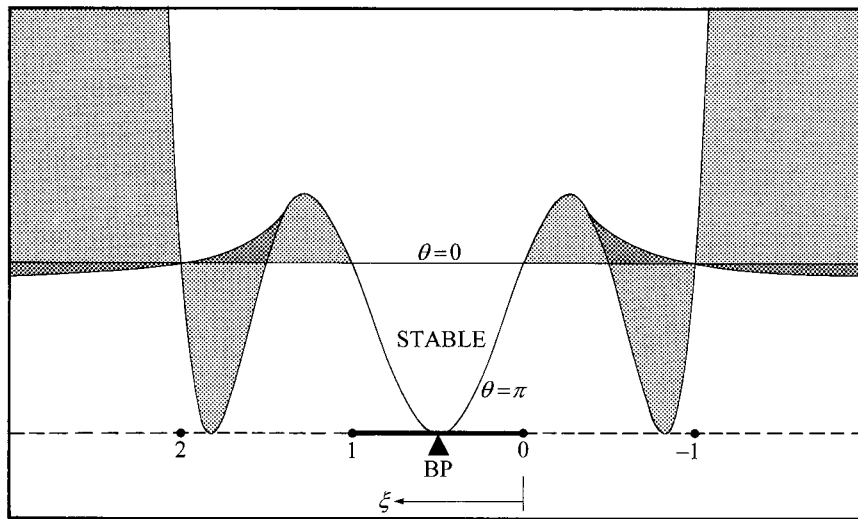


Figure B3. Third-order  $G_3^2(\xi; \theta)$  as a function of  $\xi$ , with  $\theta$  as a parameter.

*sufficient* for stability. To show that these conditions are also *necessary*, we investigate the slope of the  $G^2$  plots at  $\xi = 1$ . If this can be shown to be positive (for any order), then the above ranges of  $\xi$  are also necessary for stability (noting the respective symmetries). First, we can see from the nature of the polynomials representing  $|G_P|$  that this must indeed be the case; however, an analytical calculation will confirm this.

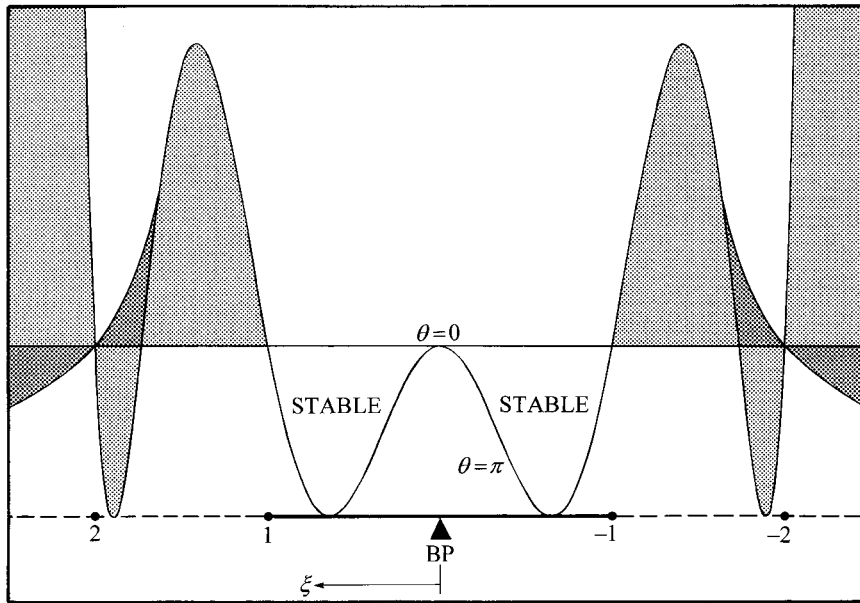


Figure B4. Fourth-order  $G_4^2(\xi; \theta)$  as a function of  $\xi$ , with  $\theta$  as a parameter.

From the general definition of  $G^2$ , Equation (B1), we have

$$\left(\frac{\partial G^2}{\partial \xi}\right)_{\xi=1} = \left(2\text{Re} \frac{\partial \text{Re}(\mathbf{G})}{\partial \xi} + 2\text{Im} \frac{\partial \text{Im}(\mathbf{G})}{\partial \xi}\right)_{\xi=1} \quad (\text{B2})$$

We know that (for any order)  $\xi = 1$  represents point-to-point transfer (from  $k-1$  to  $i$ ), in which case the local  $\mathbf{G}$  is exact

$$\mathbf{G}_{\text{num}} = \mathbf{G}_{\text{exact}} = \exp(-\mathbf{i}\theta) = \cos \theta - \mathbf{i} \sin \theta \quad (\text{B3})$$

So that we get

$$\left(\frac{\partial G^2}{\partial \xi}\right)_{\xi=1} = 2 \cos \theta \left(\frac{\partial \text{Re}(\mathbf{G})}{\partial \xi}\right)_{\xi=1} - 2 \sin \theta \left(\frac{\partial \text{Im}(\mathbf{G})}{\partial \xi}\right)_{\xi=1} \quad (\text{B4})$$

If this is positive (for some values of  $\theta$ ), we know that instability occurs (i.e.,  $G^2 > 1$ ) for  $\xi > 1$ , since  $G^2 \equiv 1$  at  $\xi = 1$ .

Consider the first-order case

$$\mathbf{G}_1 = 1 - \xi(1 - \cos \theta) - \mathbf{i}\xi \sin \theta \quad (\text{B5})$$

From Equation (B4) we get

$$\left(\frac{\partial G_1^2}{\partial \xi}\right)_{\xi=1} = 2(1 - \cos \theta) \quad (\text{B6})$$

This is positive for  $0 < \theta \leq \pi$  (and 0 for  $\theta = 0$ ), conforming to the behavior seen in the plot, Figure B1.

For second-order, we get

$$\left( \frac{\partial \mathbf{G}_2^2}{\partial \xi} \right)_{\xi=1} = 2(1 - \cos \theta)^2 \quad (\text{B7})$$

And this can now be continued to higher and higher order using the recursion relations developed in Appendix A. We summarize the results, beginning again with first-order for completeness:

$$\text{1st order: } \left( \frac{\partial \mathbf{G}_1^2}{\partial \xi} \right)_{\xi=1} = 2(1 - \cos \theta) \quad (\text{B8})$$

$$\text{2nd order: } \left( \frac{\partial \mathbf{G}_2^2}{\partial \xi} \right)_{\xi=1} = 2(1 - \cos \theta)^2 \quad (\text{B9})$$

$$\text{3rd order: } \left( \frac{\partial \mathbf{G}_3^2}{\partial \xi} \right)_{\xi=1} = \frac{2}{3}(1 - \cos \theta)^2 \quad (\text{B10})$$

$$\text{4th order: } \left( \frac{\partial \mathbf{G}_4^2}{\partial \xi} \right)_{\xi=1} = \frac{2}{3}(1 - \cos \theta)^3 \quad (\text{B11})$$

$$\text{5th order: } \left( \frac{\partial \mathbf{G}_5^2}{\partial \xi} \right)_{\xi=1} = \frac{4}{15}(1 - \cos \theta)^3 \quad (\text{B12})$$

$$\text{6th order: } \left( \frac{\partial \mathbf{G}_6^2}{\partial \xi} \right)_{\xi=1} = \frac{4}{15}(1 - \cos \theta)^4 \quad (\text{B13})$$

$$\text{7th order: } \left( \frac{\partial \mathbf{G}_7^2}{\partial \xi} \right)_{\xi=1} = \frac{4}{35}(1 - \cos \theta)^4 \quad (\text{B14})$$

$$\text{8th order: } \left( \frac{\partial \mathbf{G}_8^2}{\partial \xi} \right)_{\xi=1} = \frac{4}{35}(1 - \cos \theta)^5 \quad (\text{B15})$$

$$\text{9th order: } \left( \frac{\partial \mathbf{G}_9^2}{\partial \xi} \right)_{\xi=1} = \frac{16}{315}(1 - \cos \theta)^5 \quad (\text{B16})$$

$$\text{10th order: } \left( \frac{\partial \mathbf{G}_{10}^2}{\partial \xi} \right)_{\xi=1} = \frac{16}{315}(1 - \cos \theta)^6 \quad (\text{B17})$$

The coefficients appearing in these formulas follow from the recursive patterns outlined in Appendix A. Specifically

$$\text{1st and 2nd order: } 2 \quad (\text{B18})$$

$$\text{3rd and 4th order: } 2 - \frac{2^3}{3!} = 2 - \frac{4}{3} = \frac{2}{3} \quad (\text{B19})$$

$$\text{5th and 6th order: } \frac{2}{3} - \frac{2^2(2^2-1)}{5!} = \frac{2}{3} - \frac{2}{5} = \frac{4}{15} \quad (\text{B20})$$

$$\text{7th and 8th order: } \frac{4}{15} - \frac{2^5(2^2-1)(3^2-1)}{7!} = \frac{4}{15} - \frac{16}{105} = \frac{4}{35} \quad (\text{B21})$$

$$\text{9th and 10th order: } \frac{4}{35} - \frac{2^6(2^2-1)(3^2-1)(4^2-1)}{9!} = \frac{4}{35} - \frac{4}{63} = \frac{16}{315} \quad (\text{B22})$$

From the structure of the sequence, we see that the coefficients steadily decrease but are always positive. And, since the factor  $(1 - \cos \theta)$  ranges from 0 (at  $\theta = 0$ ) to 2 (at  $\theta = \pi$  rad), we see that the slope of the  $\mathbf{G}^2$  plot with respect to  $\xi$  is positive at  $\xi = 1$  for all non-zero wavenumbers (and, by symmetry, negative with the same magnitude at  $\xi = 0$  for odd-order schemes, and at  $\xi = -1$  for even-order).

This completes the proof that

$$0 \leq \xi \leq 1 \quad (\text{B23})$$

is both necessary and sufficient for the stability of odd-order advection schemes, and

$$-1 \leq \xi \leq +1 \quad (\text{B24})$$

is both necessary and sufficient for the stability of even-order advection schemes. This, in turn, proves that the balance point location rule is both necessary and sufficient for unconditionally stable placement of interpolation stencils for departure point evaluations in semi-Lagrangian schemes and sweep point evaluations in Eulerian schemes.

#### REFERENCES

1. Courant R, Friedrichs KO, Lewy H. Über die partiellen Differenzgleichungen der mathematischen Physik. *Mathematische Annalen* 1928; **100**:32–74.
2. Courant R, Friedrichs KO, Lewy H. On the partial difference equations of mathematical physics. *IBM Journal of Research and Development* 1967; **11**:215–234.
3. Leonard BP. Note on the von Neumann stability of explicit one-dimensional advection schemes. *Computer Methods in Applied Mechanics and Engineering* 1994; **118**:29–46.
4. Leonard BP, Lock AP, McVean MK. The NIRVANA scheme applied to one-dimensional advection. *International Journal of Numerical Methods for Heat and Fluid Flow* 1995; **5**:341–377.
5. Leonard BP, Lock AP, McVean MK. Conservative explicit unrestricted-time-step multidimensional constancy-preserving advection schemes. *Monthly Weather Review* 1996; **124**:2588–2606.
6. Roache PJ. A flux-based modified method of characteristics. *International Journal for Numerical Methods in Fluids* 1992; **15**:1259–1275.
7. Gustafsson B, Kreiss HO, Olinger J. *Time Dependent Problems and Difference Methods*. Wiley: New York, 1995.
8. Fletcher CAJ. *Computational Techniques for Fluid Dynamics*, vol. I. Springer: Berlin, 1988.
9. Staniforth A, Côté J. Semi-Lagrangian integration schemes for atmospheric models: a review. *Monthly Weather Review* 1991; **119**:2206–2223.
10. McDonald A. An examination of alternative extrapolations to find the departure point in a ‘two-time-level’ semi-Lagrangian integration. *Monthly Weather Review* 1999; **127**:1985–1993.
11. Leonard BP. Note on the von Neumann stability of the explicit FTCS convective diffusion equation. *Applied Mathematical Modelling* 1980; **4**:401–402.
12. Durran DA. *Numerical Methods for Wave Equations in Geophysical Fluid Dynamics*. Springer: New York, 1999.
13. Lax PD, Wendroff B. Systems of conservation laws. *Communications on Pure and Applied Mathematics* 1960; **13**:217–237.

14. Leonard BP. The ULTIMATE conservative difference scheme applied to unsteady one-dimensional advection. *Computer Methods in Applied Mechanics and Engineering* 1991; **88**:17–74.
15. Lax PD. Weak solutions of nonlinear hyperbolic equations and their numerical computation. *Communications on Pure and Applied Mathematics* 1954; **7**:159–193.
16. Le Roux DY, Lin CA, Staniforth A. A semi-implicit semi-Lagrangian finite-element shallow-water ocean model. *Monthly Weather Review* 2000; **128**:1384–1401.
17. Lindberg K, Alexeev VA. A study of the spurious orographic resonance in semi-Lagrangian models. *Monthly Weather Review* 2000; **128**:1982–1989.
18. Naik NH, Cane MA. An unconditionally stable scheme for the shallow water equations. *Monthly Weather Review* 2000; **128**:810–823.
19. Zubov VA, Rozanov EV, Schlesinger ME. Hybrid scheme for three-dimensional advective transport. *Monthly Weather Review* 1999; **127**:1335–1346.
20. Laney CB. *Computational Gas Dynamics*. Cambridge University Press: Cambridge, 1998.
21. Dietachmayer GS. Comments on Noninterpolating semi-Lagrangian advection scheme with minimized dissipation and dispersion errors. *Monthly Weather Review* 1990; **118**:2252–2253.
22. Leonard BP. A stable and accurate convective modelling procedure based on quadratic upstream interpolation. *Computer Methods in Applied Mechanics and Engineering* 1979; **19**:59–98.